Master of Science Thesis

A Tool for Aerodynamic Analysis of Flexible Kites

A MEMS Sensor Implementation

Bryan M.R. Franca

June 11, 2014

Faculty of Aerospace Engineering
Delft University of Technology

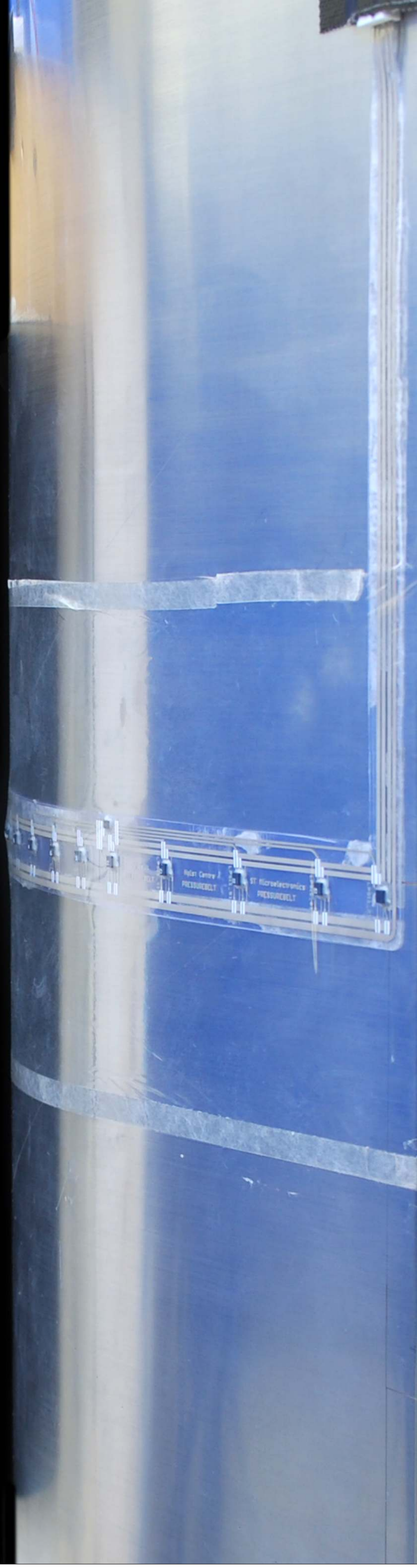

TU Delft — Delft University of Technology

Challenge the future

A Tool for Aerodynamic Analysis of Flexible Kites

A MEMS Sensor Implementation

Master of Science Thesis

For obtaining the degree of Master of Science in Aerospace Engineering at Delft University of Technology

Bryan M.R. Franca

June 11, 2014

Faculty of Aerospace Engineering · Delft University of Technology

Delft University Of Technology
Department Of
Aerodynamics & Wind Energy

The undersigned hereby certify that they have read and recommend to the Faculty of Aerospace Engineering for acceptance a thesis entitled **"A Tool for Aerodynamic Analysis of Flexible Kites"** by **Bryan M.R. Franca** in partial fulfillment of the requirements for the degree of **Master of Science**.

Dated: June 11, 2014

Head of department: ________________________
Prof.dr. G.J.W. van Bussel

Supervisor: ________________________
Dr.-Ing. R. Schmehl

Reader: ________________________
Ir. R. van der Vlugt

Reader: ________________________
Ir. W.A. Timmer

Reader: ________________________
Dr. M. Kotsonis

Summary

In recent years the global demand for sustainable energy has risen. In search of new sustainable energy sources, Delft University of Technology's KitePower group developed an airborne wind energy system. This system is based on a pumping cycle principle where a kite is reeled out with high traction forces while turning a generator, and reeled back in at lower traction forces while consuming energy. In the end, net power is produced. Research within the KitePower group has been mostly focused on the mechanical and control aspects of the system. However, recent studies within the group have shown that the system efficiency can be increased by having a better performing kite.

In search of an improved kite design the shortcomings of the current design procedures were identified. These procedures are mostly derived from the kitesurf industry where the designers have limited knowledge of aerodynamics. As a result, little is known of the kite while in-flight, such as shape, angle of attack, or even pressure distribution. Knowledge of these parameters is however essential for the validation of numerical analysis models which could be used to design and analyze kites. Additionally, the experimental data could also be used for design purposes taking into account the fact that the complexity of the numerical analysis of a flexible kite will lead to computationally intensive models, which are not recommended for use during the initial design phases.

To provide a first solution to this lack of experimental data of in-flight kites, this thesis presents the development of a system which can be used to measure the pressure distribution on the surface of a flying kite. The system is based on MEMS (Micro-Electro-Mechanical-System) barometric pressure sensors, the LPS25H by STMicroelectronics. The components are individually tested to evaluate their suitability in a pressure measuring system. Because of the barometric nature of the sensors and the requirement of the dynamic pressure for the pressure coefficient computation a pitot-static system is developed, tested, and calibrated.

The developed pressure distribution measuring system was incorporated into a flexible strip which is easy to mount onto the desired surfaces. The pressure strip was compared to the well known pressure tabs measuring method on a rigid wing section in an open jet low-speed wind tunnel at Delft University of Technology. Improvements applied to the system increased its performance resulting in a minimum pressure coefficient overestimate of 5% compared to the pressure tabs. The sensors over the middle part of the airfoil (from 15% up to 65% of the chord) showed similar response with errors of $\pm 5\%$, while at the leading edge and trailing edge of the profile larger errors were observed. The latter is explained by the larger relative thickness of the pressure strip compared to the airfoil thickness in those regions.

Acknowledgments

The idea behind this thesis work comes from my passion for kites, more specifically kitesurfing. After leaving the warmth of home and moving to The Netherlands my interest in kites lessened. Not because of the weather, winter or that wearing a wetsuit is normal, but because I would have to take a train to get to the beach. During my search for an internship, I remembered sitting on the beach back home and joking about my studies, when suggest that i should design a kite, and that is how my journey with the KitePower group started. Initially with a master orientation project which lead to an internship at Swiss Kite Power, and finally concluding with this thesis.

First of all I would like to thank Prof.dr. Gerard J.W. van Bussel and Dr. Roland Schmehl for giving me the opportunity to complete my thesis within your research group, and for your guidance and advice. To Rolf van der Vlught thank you for having the patience to cope with me, giving me feedback, and for the interesting discussions on kites.
Nando Timmer, thank you for your support and help during my wind tunnel test. Dr. Marios Kotsonis, thank you for taking the time to read my work and be a part of my graduation committee.

Without the help and support of my commercial sponsors this project would not have been possible, therefore I would like to thank Stefan Rutjens of STMicroelectronics who supported me throughout my work, not to forget your helpful connections with Holst Centre. Sebastien Marsanne thank you for your technical support. From Holst Centre I would like to thank Dr. Marc Koetse and Jeroen Schram for your help in developing and manufacturing of the flexible circuit board. Andries Bosma of Sensirion thank you for believing in my research and for your contribution.

I would like to thank my friends from Delft, for those useful study related discussions and those fun and relaxing moments. Special thanks to Lisanne en Tomas for your help during my experiments.

And last but not least the biggest thanks of all goes to my family. Without your support both morally and financially none of this would have been possible - I love you all.

Delft, The Netherlands
June 11, 2014

Bryan M.R. Franca

Contents

List of Figures

List of Tables

Nomenclature

Latin Symbols

d	Diameter	m
p	Pressure	Pa
q	Dynamic pressure	Pa
R	Acoustic resistance	$\mathrm{kgs^{-1}m^{-3}}$
Re	Reynolds number	-
U	Electrical potential	V
V	Velocity	$\mathrm{ms^{-1}}$
c_n	Normal force coefficient	-
C_P	3D Pressure coefficient	-
c_p	2D Pressure coefficient	-
T	Temperature	K

Greek Symbols

α	Angle of attack	deg
β	Elevation angle	deg
μ	Kinematic viscosity	$\mathrm{kgs^{-1}m^{-1}}$
ρ	Density	kg
σ	Standard deviation	-
ξ	Azimuth angle	deg

Subscripts

∞	Free stream

a	Ambient
ind	Indicated
ISA	International Standard Atmosphere
s	Static
t	Total

Abbreviations

ADC	Analog-to-digital Converter
AWE	Airborne Wind Energy
CFD	Computational Fluid Dynamics
GPIO	General-Purpose Input/Output
I^{2}C	Inter-Integrated Circuit
IMU	Inertial measurement unit
KCU	Kite Control Unit
KNMI	Royal Netherlands Meteorological Institute
LEI	Leading Edge Inflatable
LE	Leading Edge
LSB	Least Significant Bit
MEMS	Micro-Electro-Mechanical Systems
MSB	Most Significant Bit
ODR	Output Data Rate
PCB	Printed Circuit Board
PDK	Product Development Kit
PEN	Polyethylene-naphthalate
SPI	Serial Peripheral Interface
SSH	Secure Shell
TE	Trailing Edge

Chapter 1

Introduction

In search of alternative and sustainable energy sources, the concept of high altitude wind energy (HAWE) was born. It exploits the fact that the wind power density increases with increasing altitude, achieving a maximum at an altitude of 11km[1]. Accessing the winds at these altitudes requires a new approach as the towers supporting traditional wind turbines can not be built to those heights. This has led to the airborne wind energy (AWE) field, a collective name for new and innovative concepts trying to harvest HAWE.

1.1 Airborne Wind Energy

The different AWE systems can be subdivided into two main categories: groundgen and flygen. The category name indicates the location of the generator within the system, ground-based or airborne. The research discussed in this report will focus on the system developed by Delft University of Technology's KitePower team. This is a 20kW AWE-demonstrator based on the pumping cycle principle.

1.1.1 The Pumping Cycle Principle

A typical pumping cycle system consists of a ground station containing a winch and generator/motor, a tethered wing, and depending on the control method selected an additional kite control unit (KCU) may be required. The tethered wing varies in design, shape, and construction material depending on the research group. The Delft KitePower team currently employs a flexible kite in their system.

The pumping cycle consists of two phases: traction and retraction. The first phase is the productive part of the cycle where energy is extracted from the wind. During this flight phase the kite is flown at high angles of attack in a figure-eight pattern. The high traction force is converted to electrical power by turning a winch connected to a generator while reeling out the kite. On the contrary, the retraction phase consumes energy while the winch reels the kite back in. For this flight phase the kite's angle of attack is reduced, therefore reducing the traction force. These phases are illustrated in Figure 1.1.

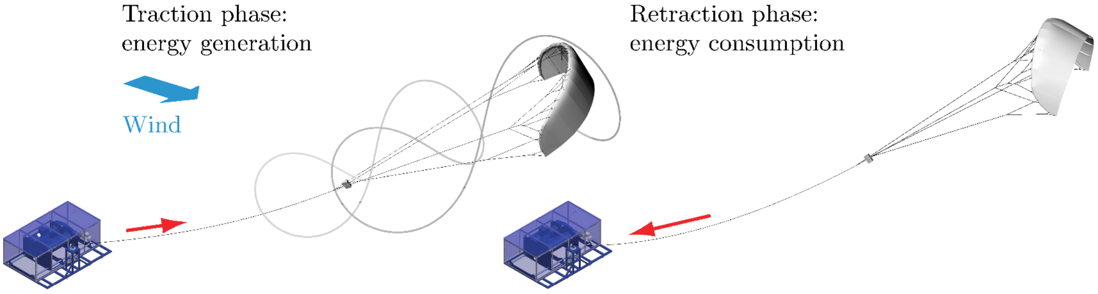

Figure 1.1: Schematic representation of the pumping cycle's traction and retraction phases for the Delft KitePower system[2].

In the end, the consumed energy is less than the produced energy resulting in net energy production. The difference between the traction and retraction force is called the de-power range of the kite. The system efficiency with respect to the kite can be increased by having higher lift-to-drag ratio[3] and/or by increasing the de-power range[4]. These improvements lead to the question,

Which kite design achieves these improvements on performance?

1.2 Research Objective

The above stated question is too broad as probably not one design will achieve all the improvements and an ultimate system will be a compromise between different improvements. So, by taking a step back and understanding the kite development and current design procedures, it can be seen that in order to achieve improvements the current qualitative kite design methodology has to evolve to a more quantitative methodology. The use of computational models and experimental data during the design process is of utmost importance to achieve this evolution. However, the lack of experimental data currently prevents this, as computational models should be validated with experimental data. The highly dynamic nature of a kite complicates the collection of experimental data, even simple parameters such as angle fo attack and wind velocities in flight are unknown. This combined with the highly flexible nature of kites resulting in unknown shapes, makes it difficult to implement computational models. Therefore an attempt is made to measure the aerodynamic forces directly on the kite, this lead to the following research objective,

The aim of this thesis is to find or develop a system that can measure the pressure distribution on a kite, both in-flight and during wind tunnel tests.

1.3 Thesis Outline

This introduction is followed by an overview of the kite history, design procedures and methodology in Chapter 2, this will highlight the short comings and obstacles in current kite designs methods. Measurement system and techniques for possible kite system implementation are discussed thereafter.

A system to measure pressure distribution is designed in Chapter 3. Additional data required are measured by a pitot-static system, which is designed and tested in Chapter 4.

The final designed product is validated against traditional pressure tabs in wind tunnel experiments, this is discussed in Chapter 5. This report is finalized with the conclusions and recommendations in the final chapter.

Additionally a method to create 3D volume kite models was developed, which can be used to perform CFD analysis and compared to the pressure measurement performed by the developed system. This method is outlined in Appendix C.

Chapter 2

Literature Review and Background Information

This chapter gives an overview of kite development not only at Delft University of Technology's KitePower team, but also the history of kites. Understanding the decisions made, and procedures used during the evolution of kites will help identify their shortcomings and possibilities for improvements. The final part of this chapter deals with the various measurement techniques and methods, and the selection of a feasible method.

2.1 Kites

Multiple definitions of a kite can be found such as the following given by the Oxford Dictionary[5]:

[From its hovering in the air like the bird.] A toy consisting of a light frame, usually of wood, with paper or other light thin material stretched upon it; mostly in the form of an isosceles triangle with a circular arc as base, or a quadrilateral symmetrical about the longer diagonal; constructed (usually with a tail of some kind for the purpose of balancing it) to be flown in a strong wind by means of a long string attached. Also, a modification of the toy kite designed to support a man in the air or to form part of an unpowered flying machine (cf. AEROPLANE n. 1).

This definition emphasizes the fact that a kite is generally seen as a toy or a modification of a toy. A kite used in energy production however, is far from a toy, Delft University of Technology KitePower team have measured pulling forces of 600kgf on the current demonstrator. Therefore, the definition given by The Cambridge Aerospace Dictionary might be a more suitable one, it reads as follows[6]:

Aerodyne (Heavier-than-air craft, sustained in atmosphere by self-generated aerodynamic force, possibly including direct engine thrust, rather than natural buoyancy.) without propulsion tethered to semifixed point and sustained by wind

A similar definition was suggested in reference [7], in which the concept of the kite as a toy is abandoned and instead the kite is considered as an aerodynamic object in the same way as we do with airplanes.

2.1.1 History of Kites

There are many theories with respect to the origin of kites, with dates of origin ranging from 9000-5000 BC[8] to around 1000 BC[9]. However, there is much more agreement on the region of origin, believed to be in Asia. Initially used for entertainment or decorative purpose, more practical uses for kites were found at a later stage. These exploited the kite's lifting capabilities and pulling force to move or lift objects. Leonardo DaVinci used a kite to span a river in the 15$^{\text{th}}$ century. Just to show the applicability and use of kites, objects lifted by them included humans, cameras, weather instruments, communications antennas, and a number of experimental setups[1]. The pulling force has been used to propel carriages and canoes forward, such as the carriage created by George Pocock[10]. Kites were also used as research and development (R&D) platforms as can be seen when the Wright brothers used tethered versions of their Wright Flyer to investigate its control and stability[11]. Although some of these kites employed multiple line steering, the breakthrough in controllable kites came in 1975 with the introduction of the Peter Powell kite, a two line steerable kite[12]. This same year another breakthrough was achieved with the introduction of the Flexifoil[13]. Up to this point kites generally consisted of flat plate lifting surfaces, whereas the Flexifoil resembled a flying wing employing airfoils copied form a glider. The Flexifoil also featured dual steering lines connected to a fiber-glass reinforced Leading Edge (LE). These breakthroughs helped define a new path in the development of kites called power kites, use of a kite for its traction force.

2.1.2 Power Kites

The further development of power kites is fueled by new sports, where a person is propelled forward on board, boat, or buggy. These kites are primarily flown on four lines, giving the pilot the ability to control the angle of attack of the kite. As the force is directly related to the angle of attack, the amount of pulling force can be directly controlled. There are two types of power kites in use today: ram-air and Leading Edge Inflatables (LEI).

Ram-air Kites

Ram-air kites are made completely out of fabric consisting of a top and bottom skin. This type of kite gets its shape from ram-air pressure recovered at inlets near the LE. The kite also has ribs similar to an aircraft wing to help maintain its desired shape. Holes through these ribs allow the air to flow span-wise giving the complete kite its shape without requiring inlets over the entire leading edge. Within the ram-air kites a distinction can be made with respect to the bridle system. There are the bridle less systems having two attachment points on either tip, one on the leading and one on trailing edge. The second

[1] The World kite altitude record was set at the Lindenberg Meteorological Observatory in Germany on August 1st 1919, using a chain of 8 kites. The highest kite reached an altitude of 9740m[14].

type the supported ram-air kites that have complex bridles, with external connections supporting most of the ribs.

Leading Edge Inflatable Kites

The Leading Edge Inflatable (LEI) kites were born out of necessity. As the sport of kitesurfing grew, the ability to re-launch the kite on water was needed. Regular ram-air kites were not able to do this[2]. The LEI development can be attributed to the Legaignoux brothers, Bruno and Dominique[15]. These kites are characterized by their inflatable frame, which consists of a span-wise leading edge beam with a number of chord-wise struts. This frame is covered by a single light weight fabric called the canopy. Due to the rigidity and flotation capabilities of the inflatable frame the kite can both maintain its shape and relaunch in water. Within the LEI kites three distinctive designs can be found.

1. **The original C-kite** given this name due to its resemblance to the letter C (almost a semi-circle). The C-kite does not feature a bridle system. The kite lines are directly connected to the tips, which featured either a carbon or inflatable strut.
2. **The bow-kite** features a much flatter shape and has a swept back leading edge. The bow-kite always features a bridle system, which supports the leading edge.
3. A hybrid version of the C-kite and bow-kite is the latest design trend. These designs may look very similar to either the C or bow kite. They will always feature a bridle system. Also known as supported C.

Both ram-air and LEI kites are steered by deformation, so maintaining flexibility of the construction is important. Both designs have their advantages and disadvantages for use in kite power production. The ram-air kite has a better defined profile shape while the LEI kite has a round LE and a single skinned aft section. Therefore, the aerodynamic performance of a ram-air kite is better than that of a LEI kite, thus achieving higher lift to drag ratios. On the other hand, the LEI kite's semi-rigid frame allows it to operate at a wider range of angles of attack compared to ram-air kites. This is due to the fact that ram-air kites use stagnation pressure to maintain their shape, in addition to their complex bridle setup. If the stagnation pressure is moved away from the inlet, the internal pressure may drop resulting in a collapse of the kite[3]. This broader angle of attack range gives better de-power capabilities to the LEI kites.

2.1.3 Kite Development within Delft KitePower

The current kites used by the Delft KitePower group are LEI kites. The choice for this type of kite is mainly based on its ability to have a larger de-power range compared to

[2] There are ram-air kites that have closable inlets, so that the kite maintains it shape and stays afloat. These were developed at a later stage

[3] In the paragliding scene, which can be compared to a ram-air kite developments have shown that the implementation of a shark nose profile increases the $C_{L\min}$ to $C_{L\max}$ range.

ram-air kites. Although, an attempt to increase the de-power range of a ram-air kite was made by implementing steering rails at the tips. However, these did not function as planned as the rails twisted and the steering mechanism jammed. A completely different approach was the kiteplane, as the name indicates a mix between a plane and a kite. Made from an inflated frame it had a double skinned wing, and the empennage consisted of a vertical and horizontal tailplane. The control of this kite was done in similar manner as an aircraft by deflecting control surfaces mounted on the empennage and wings. During test flights the kiteplane suffered from instability problems both laterally and pitch down, which made it difficult to maintain airborne. Additionally, some flutter and oscillations of the wing caused damage to the construction. These damages and crashes caused the concept to be abandoned.

The currently used LEI kite has evolved from a off-the-shelf kitesurfing kite to the current model through lessons learned during flight tests. The evolution of the Delft KitePower kite up to this point is briefly described below and are shown in Figure 2.1:

- **Ram-air kite**, an off-the-shelf Peter Lynn kite that was flown both by the rails and KCU.
- **Kiteplane**, a self-built design developed by Jeroen Breukels en Roland Verheul.
- **Version 1 (V1)**, this is basically a standard kitesurf kite designed by Mutiny. The differences are that it was scaled up to have a flat surface area of 25m^2 which is twice the normal kitesurf kite size, and reinforced to achieve higher loading.
- **Version 2 (V2)**, the lessons learned from the V1 led to more modifications. This version has a slightly different leading edge shape and two extra struts were added to better support the canopy. The bridle connection points at the LE were split into two connection points in chord-wise direction.
- **Genetrix Hydra**, this is an off-the-shelf kitesurf kite it is flatter and more slender then the V1 and V2, and it has a larger de-power range. Because of the limited size of off-the-shelf kites, the surface area of this kite is only 14m^2 and is reserved for strong wind conditions. Additionally a more complex bridle was introduced where all struts are supported at the trailing edge, in contrast to the standard bridle that only has the tips supported at the trailing edge.
- **Version 3 (V3)**, this is a scaled-up version of the Genetrix Hydra featuring the same fully supported trailing edge bridle, and was made in collaboration with Genetrix. The flat area of this kite is 25m^2. The billowed shape of the trailing edge in-flight, has been applied to the leading edge. This is an attempt to design a kite that more closely resembles the predicted shape observed during flight test.

Currently the V3 and the Genetrix Hydra are used for full system tests, depending on wind conditions. Both these kites have had their struts reinforced with carbon rods. Since the placement of multiple bridle points on the strut reduces the kite's ability to de-power, in order for a strut to transfer the loads to the trailing and leading edge bridles additional reinforcements were required.

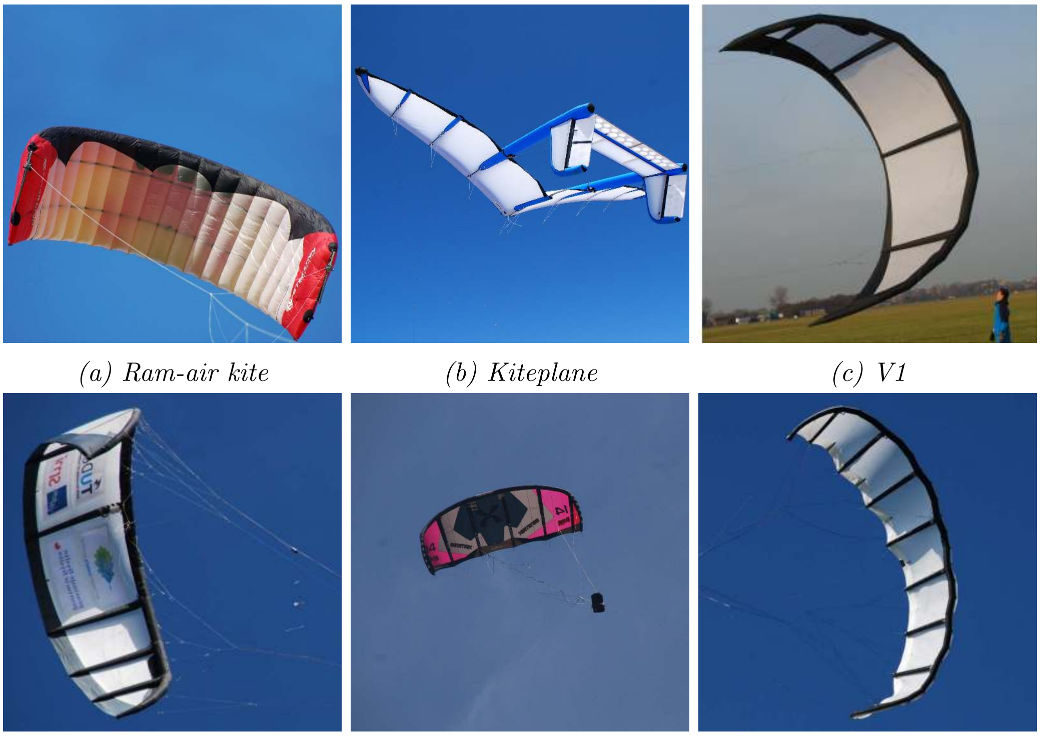

(a) Ram-air kite *(b) Kiteplane* *(c) V1*

(d) V2 *(e) Genetrix Hydra* *(f) V3*

Figure 2.1: Previous and current versions of kites used by the Delft Kitepower group.

Because the current kite used in the KitePower system evolved from kitesurfing, it is important to understand the origin of kites in general, but more specifically the kitesurfing ones. The evolution and design procedures within the kitesurf industry are of importance for the further development of the KitePower system. Therefore, the following subsection deals with these topics.

2.1.4 Kitesurf Industry

The kite design procedure currently employed by the kitesurfing industry is not as well defined and structured as the design process typically followed in the aircraft industry. It can be said that the current kite design is comparable to the aircraft design methodology during the first years of aviation even though kites have been around longer than aircraft.

Currently, kitesurfing kite designers employ a structured trial-and-error method, which has been compared to the Darwinian process of evolution[7]. Here, the designer uses personal design experience to create a batch of prototypes, which is tested by a selected group of professional kitesurfers (most commonly the team riders for that specific brand)[16]. The kitesurfers give their feedback to the designer, who tries to identify the features that gave positive feedback and uses these for a new batch of prototypes. This process may be repeated several times, until a final design is fixed. The number of parameters varied per batch may vary from one to a few depending on required results and personal preference of the designer. One of the main weakness of such a design approach is that the designer has to depend on the feedback from kitesurfers and this feedback is of a qualitative nature.

Also riding style, weather conditions, and personal preference of the riders may influence their feedback.

Design Attempts of Kitesurf Kites

From the design attempts made, both during prototyping and final product, it can be seen that the designers' knowledge of aerodynamics has evolved and expanded by incorporating knowledge from different research fields. Some examples of innovation attempts are given next:

- **Ocean Rodeo Sports INC**, designs and markets kites with so-called VENTURI TECHNOLOGY. These are vents placed around two-thirds of the chord, to help reattach the flow at high angles of attack[17].
- **Ozone Kitesurf LTD**, designed a prototype called Seagull, this kite has a similar billowed LE as the V3 kite (M shape if viewed from the front).
- **Naish Kites**, had two kite models the Bolt and the Helix that are part of the Σ series. Their leading edge is shaped like the letter Σ, it resembles a diving Peregrine falcon (omitting the head). The Peregrine falcon has the fastest recorded speed measured on a living animal at 320kmh^{-1} (200mph)[18].
- **Seasmik**, relative flat kite believed to be the first bow kite and featured good de-power characteristics. It resembles a square kite.
- **Wipika and Naish**, have attempted to make prototypes featuring either a complete or partial double skin[19].

As the kite design progressed over the years it has become harder to achieve improvements in the design, requiring ever increasing number of prototypes[7]. This brings the sustainability of the design method into question, it is currently feasible due to the relatively low cost of kite manufacturing compared to the use of computational models. The larger number of prototypes translates to increasing cost, where a point may be reached that the computational approach or a combination of the two approaches will be a most efficient solution. Comparing the evolution of kite design to aircraft deign, might suggest that kite design as it is now is reaching the end of an S-curve requiring new design methods and tools to initiate the next S-curve[25]. The transition to a quantitative method for the design of kites could facilitate this transition. The next section will deal with possible existing experimental methods to facilitate the transition of the design method to a quantitative one.

(a) Close up of the Ocean Rodeo Razor featuring the VENTURI TECHNOLOGY vents[17].

(b) Ozone Seagull[20].

(c) Naish Bolt[21].

(d) Diving Peregrine falcon[22].

(e) Naish Helix[23].

(f) Seasmik[24]

(g) Wipika double skinned kite[19].

(h) Naish kite featuring partial double skin[19].

Figure 2.2: Kitesurf kites design attempts.

2.2 Experimental Analysis

The number of quantitative experiments performed on kites is limited. Of the known experiments performed on kites none have measured the pressure distribution on the kite neither in a wind tunnel or in-flight. Therefore techniques and methods used in other research fields have to be explored for their applicability in kite research. There are a number of techniques used to measure the pressure distribution over lifting surfaces that could be suitable. Their sensitivity to environmental variables dictates whether these methods are applicable in free flight or wind tunnel environments. The use of wind tunnels allows the control of the environmental variables which in turn are important for reproducibility, in contrast to free flight testing where these variables cannot be controlled. On the other hand aspects such as wall interference, blockage, and scalability should be considered when using wind tunnels. Scalability is a consequence of the limited size of wind tunnels, requiring the use of scaled models. Not only does the reduced Reynolds number have an effect on the kite's aerodynamic behavior, the aeroelastic behavior is also influenced[26]. The additional support required to fix a kite in a wind tunnel makes the wind tunnel unsuitable for analyzing the kite's deformations, especially during maneuvering[27]. Before proceeding to the various pressure measuring methods, an overview of experiments performed on kites and on structures with similarities to LEI kites is presented.

2.2.1 Kite Experimental Research

One of the first attempts at measuring the lift and drag coefficients of a LEI kite was done through crosswind kite tests[28]. By fixing a kite to a ground anchor it was swept through the power zone while values such as tether force (force gauges), kite velocity (GPS), and wind velocity (anemometer) were measured. The measured data was converted through trigonometric relations and the estimate that the ratio of kite velocity over wind velocity is equal to the lift to drag ratio. This resulted in lift to drag ratios for the same kite varying between 4 and 6. This test setup did not define an angle of attack but instead used the force ratio between the front and back lines on the kite as a similar parameter.

A study based on the same principles as before but with the addition of an IMU (inertial measurement unit) mounted on the kite was the first attempt to produce a lift curve based on angle of attack[29]. The lift and drag curves were derived from the measured resultant force coefficient based on angle of attack. The angle of attack however, was not defined with respect to the kite geometry but was rather based on the IMU placement. Additionally this study also included the first airborne anemometer to measure the apparent wind velocity at the kite. The resultant force coefficient was found by fitting a curve through a point cloud, the fit or measurements can be argued as the spread was 0.7 on the force coefficient and 20 degrees on the angle of attack, this can be seen in Figure 2.3.

A more interesting approach combined wind tunnel experiments with CFD (computational fluid dynamics) computations[27]. By placing a ram-air kite in a wind tunnel the forces on the lines was measured while the shape was registered by photogrammetry and laser scanning. The photogrammetry setup consisted of 14 cameras requiring accurate placement and calibration in the wind tunnel, and 2000 markers on the kite's surfaces.

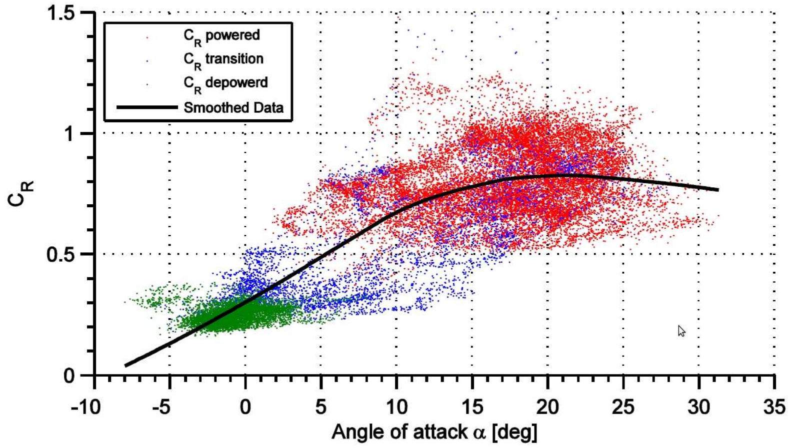

Figure 2.3: Resultant force coefficient as function of angle of attack[29].

Additional attachments besides the bridle were required in the wind tunnel due to the kite's natural instability. The reconstructed kite shape was used to perform CFD computations and results compared to the wind tunnel measurements. Interesting was also the comparison of actual flight shape versus the design shape where the ballooning and wrinkles in the kite are clearly visible. These deviations between design and flight shape can help the designer reverse engineer a design to improve its performance.

The accuracy of the photogrammetry setup in the previous experiment was less than 3mm, implementing such a setup for in-flight tests is quite complex. Not only does the number of cameras complicate the calibration process but the fact that the kite is moving requires a larger viewing area. An attempt to perform photogrammetry on actual flight test was done using tow tests[30]. By using a two camera setup the shape of the kite was determined. Due to the high curvature of the kite, having only two cameras, and the low number of areas of interest the shape determinations was not accurate. The determined shape was related to the tether force measured by a load cell. Using a reference shape of the kite at a point of least loading (0N) displacement of different parts of the kite were determined. The maximum displacement was found at the tips and was equal to 350mm for a tether force of 1,200N. However there is no mention of the accuracy of the shape determination setup, and only small data sets were available as it was difficult to maintain the kite in the cameras field of view. The difference between the designed shape and reference shape used is also unknown.

2.2.2 Experimental Research on Structures Similar to LEI Kites

Lift generating structures that have comparable airfoils to LEI kites are wings for ultra-light sailplanes, hang gliders, and man powered aircraft using membrane structures. The research performed on the Princeton sailwing showed that the variation of LE shape and partial or complete lower skin have a large impact on the performance of the wing[31]. The model consisted of a solid LE and a TE tensioning cable, while a force balance was used to measure the lift, drag, and pitching moment in a wind tunnel. It was found that the sharp LE combined with full lower skin achieves the highest lift-to-drag ratio. The variation in the TE cable tension showed better aerodynamic performance at the highest tension. The higher tension means less deformation possible in the canopy, which with current LEI designs constraining the TE might prove difficult. It should be noted that the experiment was performed in 3D, and thus is planform dependent. The author explicitly warns that variations in the wing design incurred large performance penalties, hence its direct applicability to kites is debatable. This might be the reason that double skinned LEI kites have been unsuccessful.

A study analyzing the effect of slack on a straight sailwing consisting of a single canopy and a circular LE was performed[32]. The maximum lift-to-drag ratio was achieved with different levels of slack depending on the Reynolds number. Also visible from shape images was that the location of maximum camber moves forward for the same angle of attack and slack setting with increasing Reynolds number. This would imply that the shape of a LEI kite's airfoil is constantly changing during flight.

Structural similarity can be found in the sailing world, where the mast and sail represent the LE and the canopy of the LEI kite. The relation between mast and lift-to-drag ratio found through scaled wind tunnel test, using rigid rectangular sails with Re $0.4 \cdot 10^6$, suggests that the absence of a mast results in the best lift to drag performance. But the highest achievable angle of attack is for a thick mast, with a diameter to chord ratio of 1/8 and the sail is attached to the center of mast[33]. Furthermore modifications to the twist and camber of the sail along the span gave beneficial results regarding lift-to-drag ratio. This however, might not be the case for kites due to the steering deformations required.

Different flow field regions have been identified on a sail using different methods: full-scale tests, wind tunnel test and numerical simulations[34]. All three methods show an area of detached flow behind the mast, with reattachment occurring aft and an resulting in an additional decrease in pressure coefficient. The separation bubble is mainly due to the presence of the discontinuity in the airfoil shape at the mast to sail transition. If this transition is not smooth with respect to the incoming flow a separated flow bubble may appear. This has impact on the design of the kite regarding the optimum location of the LE-canopy seam. It should be noted that these tests and simulations were done with the presence of the Genoa sail which interacts with the main sail, these interactions are not present on a LEI kite.

2.2.3 Pressure Distribution Measurement Systems

The are a number of methods to measure the pressure distribution over an airfoil. The frequently employed method uses pressure tabs connected to a pressure transducer via tubing. The tabs may be flush orifices in the skin, with the tubing running on the inside of the structure for which purpose built wind tunnel models are required. Although, full-scale tests have been performed on airplanes using flush orifices[35]. The previously mentioned sail boat wind tunnel experiment made use of these flush orifices by implementing a sandwich structure sail[34]. In contrast to this the full-scale test made use of non-flush orifices where the pressure taps were in the center of a frustum[4], and the

[4]The portion of a regular solid left after cutting off the upper part by a plane parallel to the base; or the portion intercepted between two planes, either parallel or inclined to each other[5]

tubing ran flat on the sail. Instead of having a number of individual orifices, a number of flexible tubes can be joined to create a pressure belt. One end of the tubes are closed while the others are guided to a pressure transducer. The combined tubes are wrapped in chord-wise direction around the airfoil. By making a small hole in the top part of each tube the pressure at different chord-wise locations can be measured. Additional fairings may be placed on the sides to produce a smooth transition similar to the frustum. With respect to the influence of the outer diameter of the tube it was shown that for diameters equal to 1.6mm, 3.2mm, and 4.8mm ($Re\ 3 \cdot 10^6 - 5 \cdot 10^6$), there was no noticeable difference when the results were compared to those measured by flush orifices over a large part of the airfoil[36]. There were however some discrepancies near the TE which increased with tube thickness and increasing lift. CSEM, a Swiss based research center, offers a miniature pressure belt, where 16 tubes are merged into a single strip[37]. Figure 2.4 shows the CSEM sensor unit that contains 16 differential pressure sensors and the strip containing the 16 tubes referred to as channels.

Figure 2.4: Pressure belt unit offered by CSEM[37].

A new method to measure the pressure directly is to make use of Micro-Electro-Mechanical-Systems (MEMS)[38] and capacitive sensors[39]. These are small electrical sensors that can measure the pressure variations over time, and thanks to their small size increase the possibilities to perform in-situ measurements. Combining a number of these sensors with flexible printed circuit board (PCB) makes it feasible to measure pressure distributions on curved surfaces.

There are additional measurement techniques which may be classified as optical systems. One of these uses pressure sensitive paint, which is widely used in wind tunnel tests and has been implemented in aircraft flight tests[40]. However if this technique is to be applied outdoors it requires the test to be performed during moonless nights. Also, its sensitivity to pressures at velocities below 50ms^{-1} is quite poor[41].

2.2.4 Kite Pressure Distribution System Selection

Due to the nature of the kite construction, design, and flight path there are a number of hard constraints on the measurement technique and system to be used, with the weight and size of the system being the main ones. Because of their weight, size, and platform inconsistency the use of optical measurement system is deemed infeasible for in-flight measurements on kites.

Because the current LEI kites lack a lower skin to allow the tubing to be hidden, as not to interfere with the flow, flush orifices are also considered unsuitable. This leaves the option of either a pneumatic pressure belt system such as the one offered by CSEM, or an electrical measurement unit which using MEMS or capacitive sensors. The main disadvantage of the pneumatic system is that it makes use of long tubing which suffers from acoustic and viscous lag[38]. The lag is a problem for the implementation of in-flight kite testing, as the flight is highly unsteady. This unsteadiness for a figure-eight maneuver is illustrated in Figure 2.5, where it is clear that the tether force varies constantly hence the aerodynamic behavior of the kite also varies.

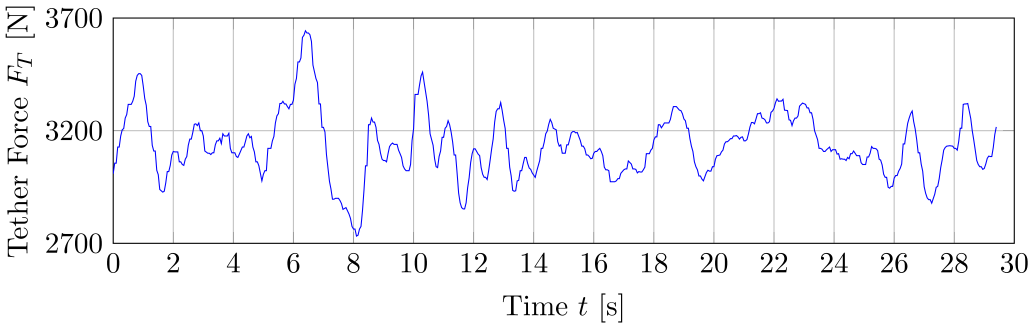

Figure 2.5: Tether force of the Delft KitePower V3 kite while flying a single figure-eight maneuver.

In order to estimate the time response of a pneumatic system placed on the V3 kite, use is made of the wave model[42] described by the following equation;

$$\frac{\mathrm{d}^2 P_L(t)}{\mathrm{d}t^2} + 2\xi\omega_\mathrm{n}\frac{\mathrm{d}P_L(t)}{\mathrm{d}t} + \omega_\mathrm{n} P_L(t) = \omega_\mathrm{n}^2 P_0(t) \tag{2.1}$$

Here $P_L(t)$ is the pressure response at length L, the input pressure is given by $P_0(t)$, and ω_n and ξ are defined as:

$$\omega_\mathrm{n} = c\sqrt{\frac{A_\mathrm{c}}{LV_\mathrm{e}}} \tag{2.2}$$

$$\xi = \frac{R}{2\rho_0\omega_\mathrm{n}} \tag{2.3}$$

With c representing the speed of sound, A_c the tube cross-sectional area, L the tube length, ρ_0 the density. V_e is the effective volume of the pneumatic system, including the tubing volume V_tube and sensor volume V_sensor, and is computed as follows:

$$V_\mathrm{e} = V_\mathrm{sensor} + \frac{V_\mathrm{tube}}{2}$$

For the current situation of simply analyzing the tube delay the sensor volume is assumed to be equal to zero. The acoustic resistance R for laminar flow is given by[43]:

$$R = \frac{32\mu}{d^2}$$

Where μ indicates the kinematic viscosity and d the internal tube diameter. The transfer function of the tube system $H(s)$, is obtained by applying the Laplace transform to

Equation (2.1) written as the ratio of response over input as indicated by Equation (2.4)

$$H(s) = \frac{\mathcal{L}\{P_L(t)\}}{\mathcal{L}\{P_0(t)\}} = \frac{\omega_{\mathrm{n}}^2}{s^2 + 2\xi\omega_{\mathrm{n}}s + \omega_{\mathrm{n}}} \tag{2.4}$$

Knowing that the center chord of the V3 kite equals 2.70m and accounting for additional tubing to wrap around the LE, a maximum tube length of about 3m can be assumed. The response to a step input of a tube of 3m with varying diameters is given in Figure 2.6. The minimum response of such a system is obtained for diameter equal to 1.25mm

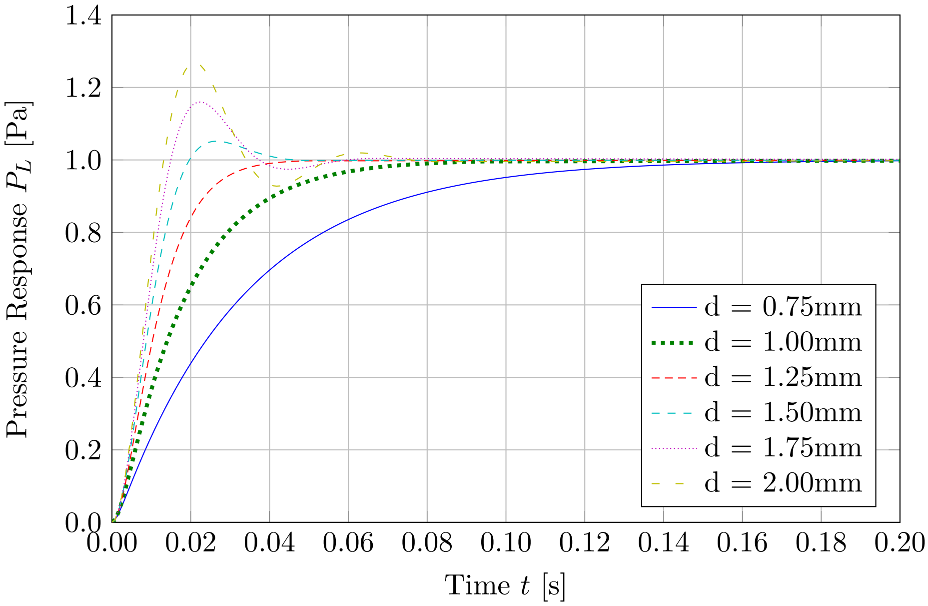

Figure 2.6: Response for a tube of 3m with variation in diameter to step input $P_0(0) = 1$.

and is equal to 0.05s or about 20Hz. In-flight deformations of the kite can cause tubing to deform and or kink which in turn induces a change of the internal diameter. If the deformation causes a reduction in the cross sectional area of more than 50%, significant additional delays are introduced[44]. The use of differential pressure sensors requires a reference pressure to be connected to the unit. This can either be a sealed container with a known pressure or a reference tube to a point of undisturbed flow around the kite. A point of undisturbed flow will require long tubing through the bridles and the pressure canister might need temperature compensation as kite altitude may vary during the measurements.

On the other hand, the electrical system will not suffer from pressure lag as it will be an in-situ system. The use of an absolute pressure sensor might require additional calibration runs in order to be able to compute the differential pressure, and also the measured value is a factor 10^3 larger than the desired value. This magnitude difference can introduce large errors in the results. The absolute sensor does not require a connection to a reference pressure during measurements, thus avoiding both the pressure canister and long tubes through the bridles. Additionally flexible circuit boards are less sensitive to bending, as the measured value is not dependent on the shape of the circuit. The sensor package size is constantly reducing while the performance is increasing (see Table 3.1 for subsequent models of ST Microelectronics).

Based on these advantages and disadvantages of the two possible pressure measurement systems it was decided to develop an electrical pressure measurement system for the kite. Additionally the electrical system has a large technological growth potential while pneumatic systems' performance is limited by a number of physical phenomena which do not occur in the electrical system. The rest of this thesis will focus on the development and validation of this electrical pressure measurement system.

Chapter 3

Pressure Distribution Measuring System Design

In the previous chapter it was elected to design an own electrical pressure measurement unit for the kite. In order to convert the measured pressure distribution into the pressure coefficient the following equation is used[45],

$$C_p = \frac{p - p_\infty}{q_\infty} \tag{3.1}$$

The pressure p is sensed by the pressure measurement unit placed on the kite surface, while the free stream dynamic pressure q_∞ and the static pressure p_∞ will be measured separately. The free stream values and its measurement system will be discussed in Chapter 4. This chapter will discuss the selection and validation of the chosen surface mounted pressure measuring sensor, in addition to the data acquisition system and data structure.

3.1 Sensor Selection

The sensors considered for the system at hand were narrowed down to complete digital units. In which each single unit package should contain all the required components, and the data should be transmitted as a digital signal. All considered models are listed in Table 3.1. All of the sensors are temperature compensated and operate on either the I^2C (Inter-Integrated Circuit) and SPI (Serial Peripheral Interface) buses. The final selection was based on accuracy and dimension. The dimension is important as a large footprint will constrain the curvature that can be matched by the system and the height will cause a larger disturbance to the flow. The LPS25H manufactured by STMicroelectronics was

[1] At the time of selection the LPH25H was in prototype phase, but was still offered by the manufacturer for this project.

Table 3.1: Specification of the different MEMS sensors considered.

Brand	**Model**	**Range [hPa]**	**Absolute Accuracy ±[hPa]**	**Resolution [hPa]**	**Noise [hPa]**	**Dimension [mm]**		
						l	**w**	**h**
Bosch	BMP180	300-1100	1	0.010	0.03	3.60	3.80	1.00
ST	LPS331AP	260-1260	0.2	0.020	0.02	3.00	3.00	1.00
	LPS25H[1]	260-1260	0.2	0.010	0.01	2.50	2.50	1.00
Measurement Specialties	MS5611	10-1200	1.5	0.012		3.30	5.00	1.00
	MS5607	10-1200	1.5	0.024		3.30	5.00	1.00
	MS5561C	10-1100				4.75	4.25	1.68
Freescale	MPL3115A2	500-1100	4	0.015	0.015	3.00	5.00	1.10

selected. This sensor has an internal piezoresistive silicon membrane spanned over a cavity. The sensor has multiple built-in features which are of interest for the pressure distribution measurement system:

- Output Data Rates (ODR) modes: One shot, 1Hz, 7Hz, 12.5Hz, 25Hz[2].
- Internal averaging mode: the number of internal samples taken per output 8, 32, 128, 512.

More information on the sensors mechanical and electrical specifications can be found in the data sheet in Appendix A. The ideal operation mode of the sensors is investigated during the sensor validation. Before the validation process can be explained, the necessary equipment and facilities used for the sensor validation are elaborated on.

3.2 Sensor Interface and Testing Equipment

The LPS25H sensors used for the preliminary validation were mounted on prototype PCB's as shown in Figure 3.1. As mentioned in the previous section these sensors can function both on SPI and I^2C bus, but the delivered prototype sensors boards were configured for the I^2C bus.

In order to control and log the sensor data, a single-board computer was used. The reason for selecting a single-board computer is to maintain the weight and size of the complete measurement system to a minimum, in order to facilitate in-flight measurements. For this purpose a Snowball-PDK (Product Development Kit) produced by ST-Ericsson was used (see Figure 3.2). The main features of the Snowball are build in GPS, accelerometer and I^2C bus at 1.8V including pull-up resistors. The GPS will be used to time stamp the pressure measurement data so that during post-process it can be synchronized to the main kite system data (for information regarding kite system data see Reference [2]). The presence of a built-in I^2C bus with pull-up resistors eliminates the need of creating one by

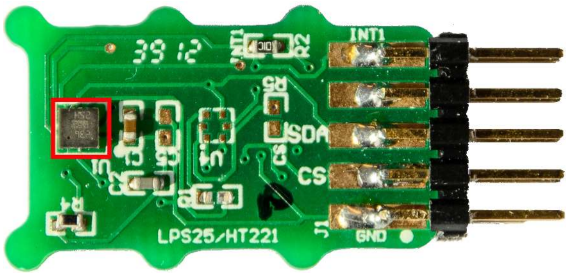

Figure 3.1: Prototype LPS25H pressure sensor highlighted in red mounted on prototype PCB that was used for sensor validation.

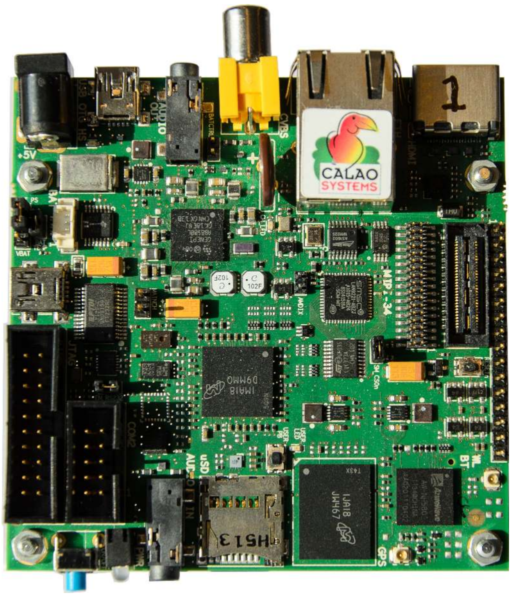

Figure 3.2: Snowball the single-board computer used to control and log sensor data.

programming the general-purpose input/output (GPIO) pins of the Snowball computer.

The supply voltage available on the Snowball was 4.5V which is beyond the operational voltage required for the pressure sensor. To reduce the voltage to within the operational range of the sensor a voltage regulator was required, that dropped the voltage to 1.8V as this is equal to the I^2C operational voltage. The schematic drawing of the voltage regulator circuit can be found in Appendix Figure B.1. The Snowball operates a full version of Linux Ubuntu, and can be connected directly to a monitor and input peripherals. For this purpose it was operated through a host computer either through serial or SSH (Secure Shell) connection.

The pressure data is read through a program written in C. Pressure data is stored as three bytes on the sensor, which are read out separately. Data bytes are transmitted as MSB (most significant bit) first. Although the LPS25H features a multiple bytes reading mode, this was not used for the validation tests, as this was discouraged by the sensor manufacturer. The reason being that the validation sensors were still prototypes and

[2] According to the sensor manufacturer ODR higher then 25Hz can be reached by using One Shot mode sequentially.

could therefore not handle this feature properly. The three pressure data bytes form a 24 bit two's complement pressure output, which converted to pascal as follows:

$$p = \frac{{}^{23}|\text{byte 2}|\text{byte 1}|\text{byte 0}|^{0}}{40.96} \tag{3.2}$$

A pressure vessel was required to validate the sensors, as the sensors do not have an attachment point for a hose. The pressure vessel was created from a film canister. As can be seen in Figure 3.3 the electrical wires were sealed with hot-glue to the lid of the canister, while a hose connector was attached to the bottom with special double compound glue.

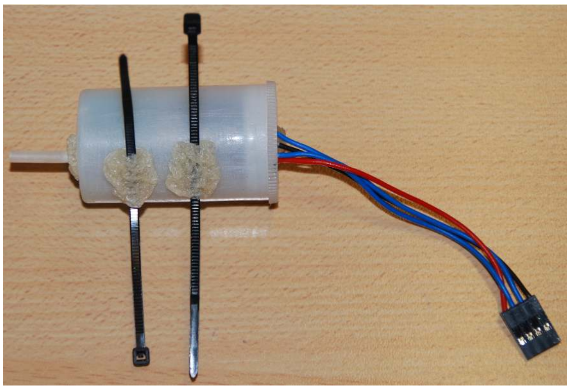

Figure 3.3: Pressure vessel created from a film canister to hold the LPS25H prototypes.

For the simulation of flow conditions during flight use was made of the M-tunnel. This wind tunnel is a hybrid tunnel as it can be operated both as a open-jet and closed wind tunnel. For the purpose of this thesis the wind tunnel was operated as an open jet for which it has a maximum operating velocity of 35ms^{-1}[46]. The test section of the M-tunnel is a square with dimensions 0.4m by 0.4m. The wind tunnel is shown in Figure 3.4.

Figure 3.4: M-tunnel at the faculty of Aerospace Engineering[46].

Additionally a stable and calibrated pressure measurement device was required to compare the performance of the LPS25H with. There were two models of digital manometers present in the wind tunnel lab. Both manometers had a pressure range of 0-2500Pa and were manufactured by MENSOR®. One of the manometers was the 2101 digital pressure gauge shown in Figure 3.5a which has a full-scale accuracy of 0.010%, while the second manometer was the 2400 digital pressure gauge shown in Figure 3.5b it has a accuracy of 0.030% full-scale accuracy.

(a) Series 2100[47].

(b) Series 2400[48].

Figure 3.5: Digital pressure gauges by MENSOR® used during wind tunnel tests.

3.3 Sensor Validation Tests

The sensor validation process was performed on multiple prototype sensors. This is done to verify that the sensors function according to the manufacturer's specifications. Validating multiple sensors ensures that manufacturing errors or PCB assembly damages can be accounted for and do not influence the outcome. It should be noted that the sensors used were from a prototype batch of the manufacturer and may still not work properly. The validation process was split into two different tests. The first test was performed to validate the static and long term response of the sensor. The second test was used to analyze the sensor response to pressure changes.

3.3.1 Sensor Static Test

For the static test a sensor was placed in the canister. The hose connection of the canister was closed off. A sample size of 25,000 at 25Hz was taken for the four different internal averaging modes.

The results for one sensor are given in the form of histograms in Figure 3.6. Each histogram has its corresponding normal distribution fit also plotted. The values for the standard deviation and the bandwidth of the data are given in Table 3.2.

From these results in can be seen that the internal averaging indeed decreases the standard deviation of the data. Comparing the accuracy of the measurements with the specifications of the manufacturer in Table 3.1 with an exception of an internal average of eight samples 99% of the measurements are within the specified accuracy of ±20Pa. Due to

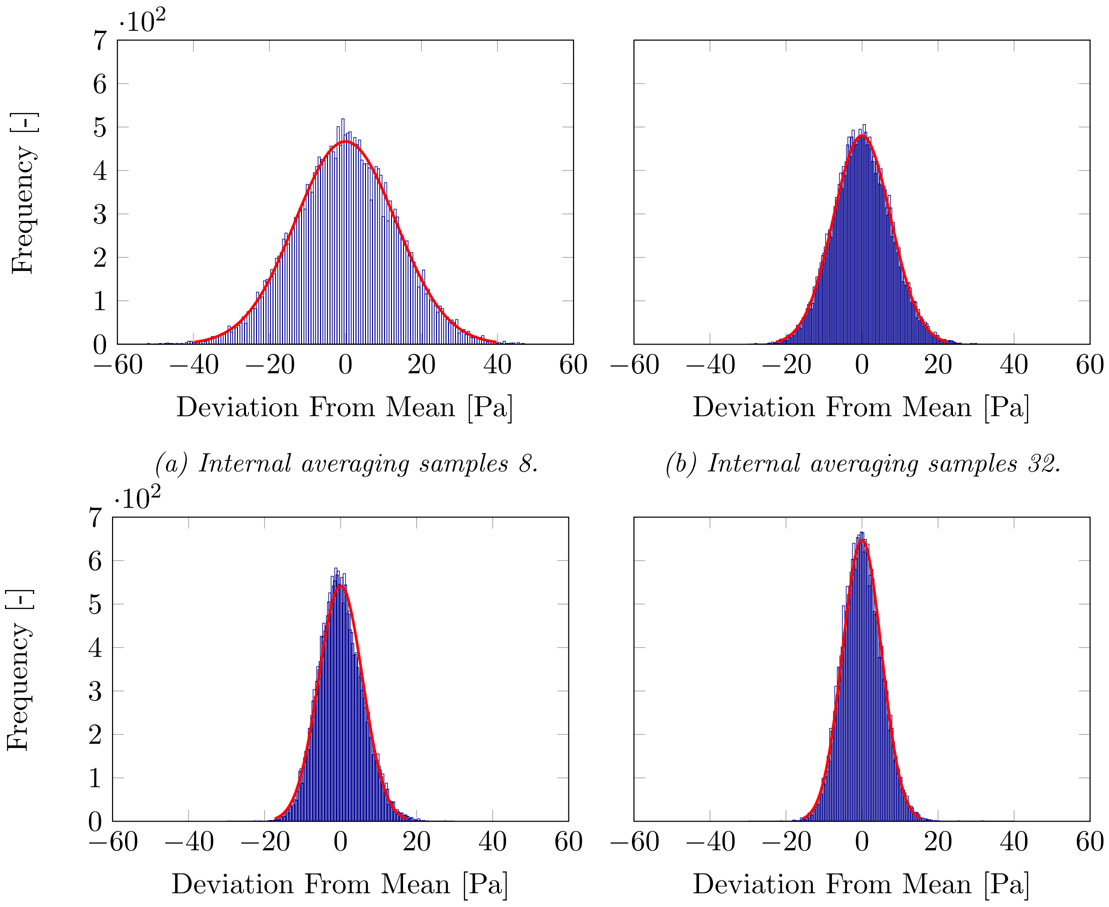

(a) Internal averaging samples 8.

(b) Internal averaging samples 32.

(c) Internal averaging samples 128.

(d) Internal averaging samples 512.

Figure 3.6: The histogram and normal distribution fit for the different internal averaging modes at 25000 samples.

close proximity of the results of both the 128 and 512 internal averaging samples, the 128 internal averaging sample mode will be used for subsequent measurements as it operates at a higher output rate.

3.3.2 Sensor Response Test

The M-tunnel was used to generate different pressures on the LPS25H sensors. This was achieved by sensing the total pressure of the flow by pitot tube in the wind tunnel. Using a T-joint the total pressure was connected to both the film canister containing a LPS25H and the wind tunnel manometer (DPG 2101). The reference pressure of the wind tunnel manometer was left open to the ambient pressure. The experimental setup is shown schematically in Figure 3.7.

The computation of the differential pressure with the MEMS sensor is similar to the intended operational procedure for the complete system. In order to measure the same differential pressure as the wind tunnel manometer the ambient pressure was measured

Table 3.2: Data analysis for static sensor testing with different internal averaging modes.

Number of internal averaging samples	**Standard deviation σ [Pa]**	**Data spread [Pa]**	**Accuracy $\pm$ 20Pa**
8	13.2	99.2	86.87%
32	7.5	58.2	99.19%
128	5.8	50.3	99.94%
512	5.1	53.3	99.98%

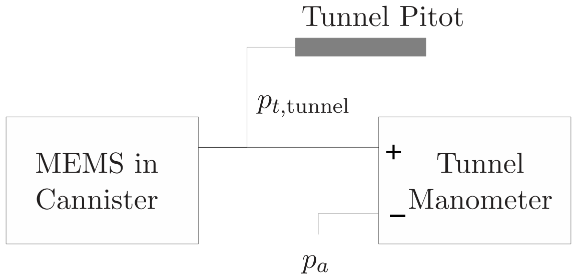

Figure 3.7: Schematic differential test setup to validate the performance of the LPS25H sensors.

with the LPS25H sensors prior to starting the wind tunnel, this is defined as $p(0)$. Assuming that the static pressure of an open jet wind tunnel is equal to the ambient pressure, the dynamic pressure of the flow is equal to the value measured by the wind tunnel manometer q_{mensor}. The flow dynamic pressure can be computed from the measurement of the LPS25H sensors with Equation (3.3).

$$q_{\text{MEMS}}(v) = p_{\text{tot}}(v) - p(0) \tag{3.3}$$

The results of both measuring methods are subtracted to define the measurement error of the MEMS differential pressure sensor setup $\epsilon_{q,\text{MEMS}}$.

$$\epsilon_{q,\text{MEMS}} = q_{\text{MEMS}} - q_{\text{mensor}} \tag{3.4}$$

The cumulative standard deviation for the dynamic pressure measured by the LPS25H sensor setup is computed with Equation (3.5)

$$\sigma^2_{q,\text{MEMS}} = \sigma(0)^2 + \sigma(v)^2 \tag{3.5}$$

The results of the differential pressure sensor setups are given in Figure 3.8 and Table 3.3 for the seven different LPS25H sensors[3].

From Figure 3.8 it can be seen that the most of the sensors with exception of numbers two and four remain within ±10Pa of the Mensor data. The sensors two and four show a large jump at the first measurement point and thereafter a rather similar graph to the other sensors. The large jump can be attributed to wrongfully taken calibration measurement

[3] There were initially eight sensors supplied by the manufacturer, these were numbered 1 through 8. However in the course of the test sensor # 5 stopped functioning. The sequential number is however kept as all data is stored using the given sensor ID number.

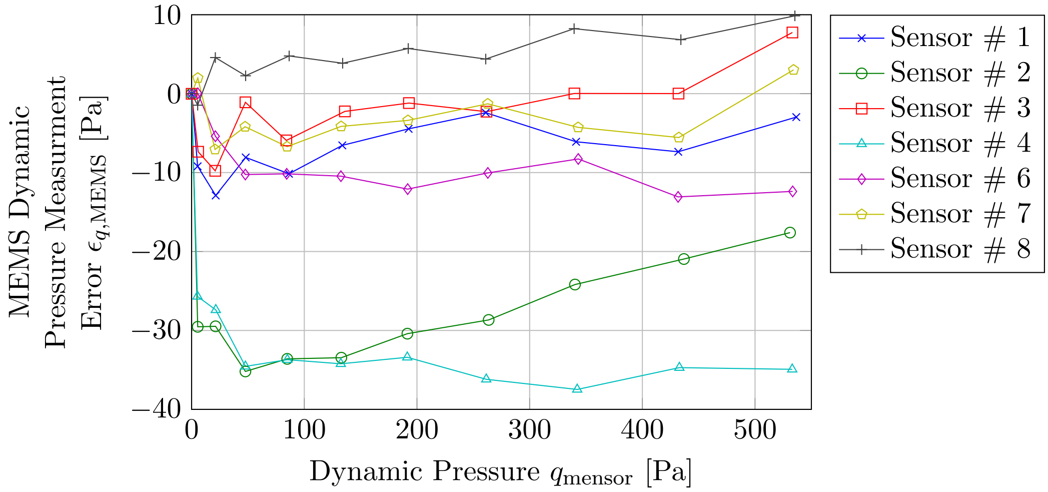

Figure 3.8: Dynamic pressure error of the differential pressure sensor setup using different LPS25H sensors.

Table 3.3: Standard distribution of the differential pressure sensor setup using different LPS25H sensors.

Sensor ID number	1	2	3	4	6	7	8
Minimum [Pa]	6.97	5.40	5.09	5.45	6.86	6.47	5.82
Maximum [Pa]	7.82	6.44	5.92	6.75	7.88	7.51	6.96
Mean [Pa]	7.39	5.70	5.51	6.06	7.23	6.88	6.26
Median [Pa]	7.32	5.66	5.44	5.99	7.19	6.85	6.28

$p(0)$. The differential standard deviations given in Table 3.3 show that the sensors perform better than sensor 1 which was used in the static test. In addition, the mean being higher than the median for all sensor indicates that there are some outliers on the high side while the data is closer on the lower side. The final deviation of around 7Pa on measured values of $1 \cdot 10^5$Pa is relatively low. And the error of $\pm$10Pa results in errors lower than 10% for dynamic pressures higher then 200Pa.

The sensors are deemed worthy of their implementation on pressure distribution measuring system. However, it should be taken into account that their constant error can produce large errors when low pressure differences are measured. Therefore their application would be more feasible at higher dynamic pressures or forces.

3.4 MEMS Pressure Strip Design

To facilitate the implementation of the LPS25H sensors as a pressure distribution measurement system, a sensor array was developed. The array facilitates the placement of the sensors on the wing of which the pressure distribution is required while maintaining wiring and additional elements to a minimum. The potential number of sensors in an array depends on the communication model used to control and acquire the sensors data. As the communication bus for the previous test was the I^{2}C this same bus will be used for the array. The are different possibilities for connecting multiple LPS25H sensors on a I^2C bus, some of the possibilities are as follows:

1. Up to two sensors can be placed directly on one I^2C bus. This is limited because the LPS25H uses 8-bit addressing and the least significant bit (LSB) of the address can be either 1 or 0 depending on the value on the SA0 pin.
2. IO-expanders can be used to manipulate the LSB of multiple sensors. Eight and sixteen bit IO-expanders are available from STMicroelectronics, allowing one sensor per bit. Different addressing of the I0-expanders allow multiple IO-expanders on the same I^2C bus, multiplying the number of sensors.
3. Two sensors can be connected to a slave micro-controller. Multiple micro-controllers can be used to create and array.

Option one is considered inadequate, as two sensors are insufficient to measure proper pressure distributions. While the IO-expanders do allow multiple sensors on the same I^2C bus, the number is still limited by the amount of ports available. The use of multiple micro-controllers allows a much higher number of sensors on the same bus. However the use of multiple micro-controllers add an extra component for every two sensors while the IO-expanders add one component for every eight or sixteen sensors to the circuitry. Therefore the second option was chosen. The selected IO-expander was the STMPE801 eight bit expander by STMicroelectronics. This expander features an address configuration pin, allowing two different addresses. Two addresses allow two IO-expanders which brings the total to sixteen sensors in the circuit. The schematic circuit drawing can be found in Appendix Figures B.2 and B.3, including the additional capacitors required for proper functioning of the sensors.

3.4.1 Pressure Strip Layout

The placement of the sensors determine the accuracy to which the pressure distribution can be determined. Although the intention is to implemented this sensor array on a kite, its implementation will be first validated on a wind tunnel wing section. Therefore the spacing for this strip was based on the shape of the pressure distribution of the wing section. The chosen wing section is straight and has a span of 1.25m and a 0.25m chord. The section consisted of only one airfoil namely the NACA-64418. Because only one pressure strip will be used during the wind tunnel validation it is decided to place it on the upper surface of the wing. Therefore the subsequent calculations are only based on the upper surface distribution.

The panel code program Xfoil was used to analyze the pressure distribution on the NACA-64418. Because this type of airfoil is a laminar flow airfoil, the placement of the pressure measurement unit will disturb the flow and function as a trip-strip. Therefore during the Xfoil analysis the flow was forced to transition. The parameters used for the Xfoil analysis are given in Table 3.4.

Table 3.4: Xfoil settings for analysis of NACA-64418 airfoil.

Angle of attack [deg]	0, 2, 4, 6, 8, 10
Mach number	0
Reynolds number	$0.5{\cdot}10^6$
Forced transition [x/c]	0.03
Panels upper/lower surfaces	103

The low number of sensors on the strip will result in a low resolution of the measured pressure distribution. The lower resolution translates to an error for the computed normal force coefficient c_n. The normal force coefficient is computed by integrating the pressure coefficient over the chord using the trapezoidal rule as given by Equation (3.6).

$$c_n(\bar{x}, \bar{c_p}) = \sum_{i=1}^{N-1} (x_{i+1} - x_i) \left(\frac{c_{p,i+1} + c_{p,i}}{2} \right) \tag{3.6}$$

In Equation (3.6) the vectors x and c_p are the Xfoil results while N is the number of measuring points. The number of measuring points for the Xfoil data is equal to the number of panels and for the MEMS measuring strip this is equal to the number of sensors. If a perfect sensor is assumed then the value measured will be equal to the Xfoil value for that given chord position. The error is thus defined as the difference between the normal force coefficients for the Xfoil and MEMS systems defined by Equation (3.6). An illustration of this error is given in Figure 3.9, where the MEMS sensors are equally spaced on the airfoil chord.

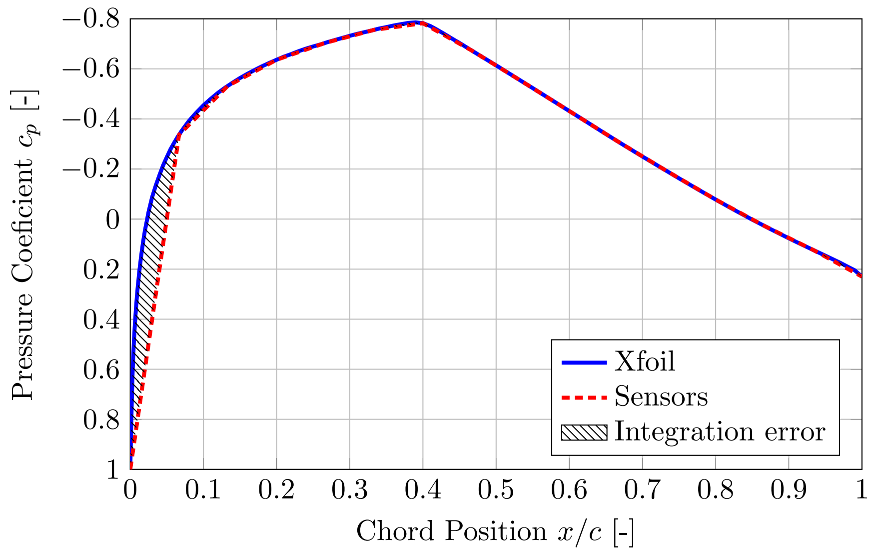

Figure 3.9: The integration error when sixteen pressure sensors are equally spaced on the NACA-64418 airfoil upper surface at an angle-of-attack of 0°.

The best sensor locations are determined by minimizing the error of the normal force coefficient for the range of angle-of-attacks (see Table 3.4) with the following minimization problem:

$$\min f(\bar{x}) = \sum_{i=0}^{5} |c_n(\bar{X}, \bar{c_{p,2i}}) - c_n(\bar{x}, \bar{c_{p,2i}})| \tag{3.7}$$

In the minimization problem $\bar{x}$ is the design vector, containing the chord location of N sensors. $\bar{X}$ are Xfoil panel locations, $c_{p,\alpha}$ is the pressure coefficient distribution for the given angle-of-attack α. The minimization problem is subjected to the following bounds:

$$0 \leq x_i \leq 1 \tag{3.8}$$

Ensuring that the sensors are placed within the airfoil chord. Additionally there are the following constraints:

$$\bar{A}\bar{x} \leq \bar{b} \tag{3.9}$$

$$\int_{x_1}^{x_N} \sqrt{1 + [g'(x)]^2} dx \leq \frac{24}{25} \tag{3.10}$$

The linear constraint in Equation (3.9) enforces a minimum spacing ($d_{\min}$) between the sensors. $\bar{A}$ is a $N-1 \times N$ matrix and b is a $N-1 \times 1$ vector and are defined in Equation (3.11). Equation (3.10) is a consequence of the manufacturing process, which currently limits the maximum length of the prototype strip to 25cm. However, the maximum distance between the first and last sensor on the strip was decided to be 24cm in order to account for routing space needed for the sensors. Therefore the arc length of the upper surface of the airfoil between the first and last sensor has to be less or equal to 24cm. And the function $g(x)$ defines the y-coordinate of the upper surface of the NACA-64418.

$$A_{ij} = \begin{cases} 1 & \text{if } i = j \\ -1 & \text{if } i+1 = j \\ 0 & \text{otherwise} \end{cases}, \; b_i = -d_{\min} \tag{3.11}$$

The final sensor spacing is based on an optimization for twelve sensors ($N = 12$). With the manual addition of the remaining four sensors at the front and the expected maximum pressure coefficient location resulted in the design shown in Figure 3.10. Note that the spacing was rounded to the millimeter.

The PCB routing and assembly were performed by Holst Centre, which is a collaboration between TNO (Netherlands Organization for Applied Scientific Research) and Imec (Interuniversity Microelectronics Centre). The final product is shown in Figure 3.11. The PCB is made from 125μm PEN (polyethylene-naphthalate) film produced by Dupont Tejin Films. The sensors are fixed using special conductive glue and the routes are printed with silver ink. The final thickness at a sensor is 1.25mm.

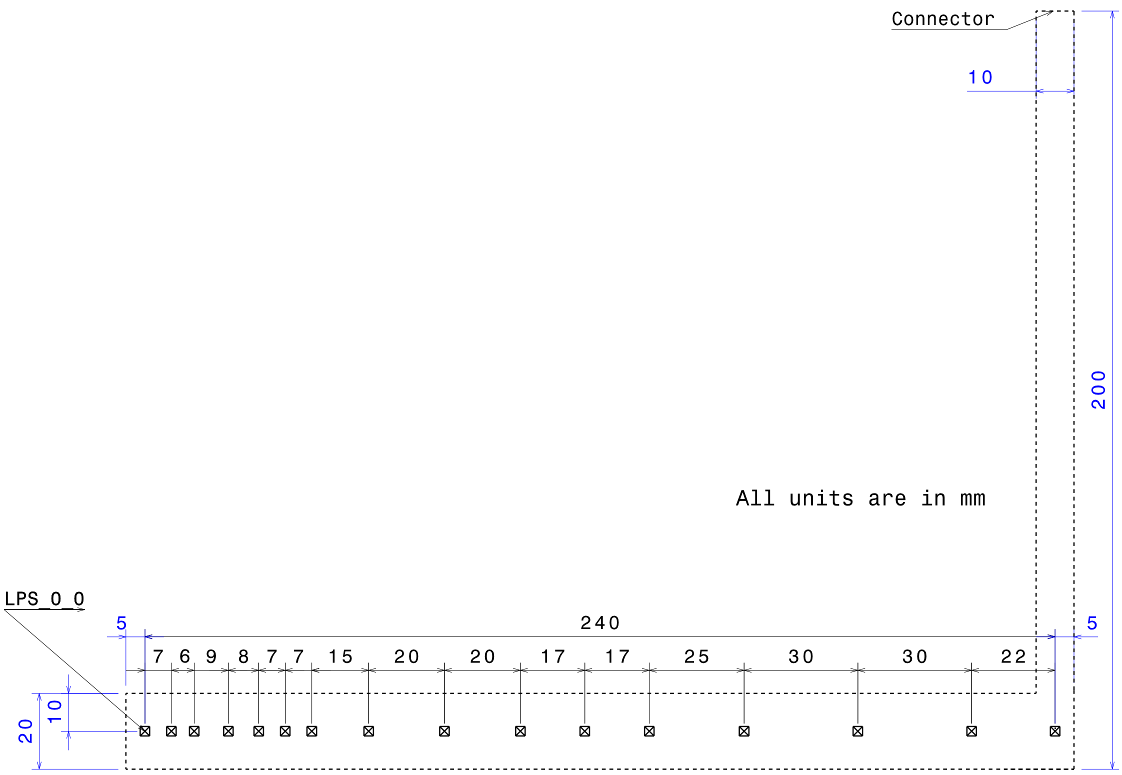

Figure 3.10: Final pressure sensor strip design.

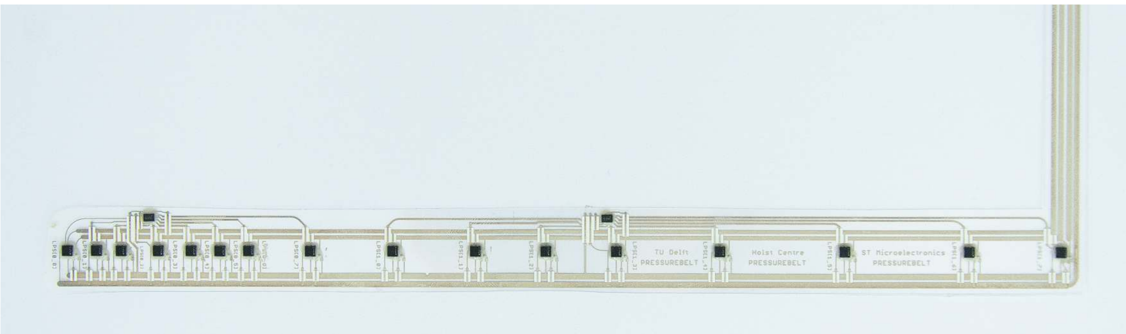

Figure 3.11: Assembled PCB featuring sixteen LPS25H sensors and two STMPE801 IO-expanders.

3.5 System Data Acquisition and Output Rate

Through the validation process of the LPS25H sensors use was made of single sensors. In order to read multiple sensors using the the IO-expanders, a different structure of the sensors control program was required. As briefly explained in the Section 3.4 the IO-expanders are used to manipulate the address pin of the sensor. When a command is sent multiple sensors can have the same address (status of the address pin), while for reading only one sensor should have the required address. Therefore, the One-Shot mode is used where the measure command is sent to all available sensors, and thereafter the data from each sensor is read individually. The structure of the data acquisition can be seen in Figure 3.12. For the current system N=2 and M=16. To ensure that each sensor has properly completed its measurement, the status of each sensor is checked prior to accessing the measured pressure data. What was noticeable was that, although the sensor itself takes some time to perform a measurement, the data collection from the different sensors slowed down the rate at which the data can be acquired. The results of the output rates for the different internal averaging modes can be found Table 3.5. As mentioned in Section 3.2 the data was initially read in through three different data transactions, however the LPS25H used on the sensor strip were final production units and thus the multiple bytes read mode could be implemented. The multiple byte read method improves the data output rate compared to the single byte read mode. The additional data acquisition loops required when multiple sensors are implemented has the largest impact on the system output rate.

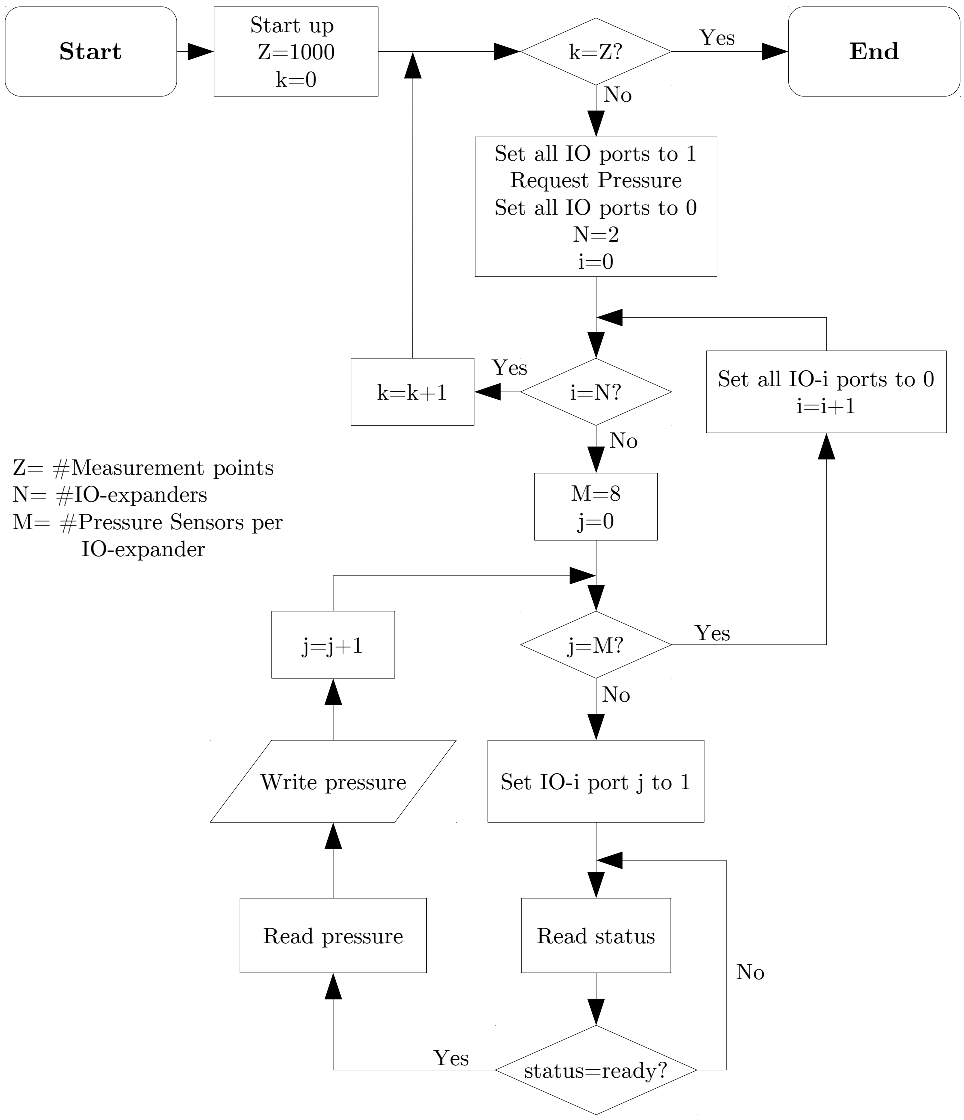

Figure 3.12: Data acquisition structure.

Table 3.5: The achieved data output rate for varying internal averaging setting.

Nr Sensors	Byte read mode	Internal average mode			
		8	**32**	**128**	**512**
1	single	206Hz	158Hz	82Hz	27Hz
	multiple	269Hz	180Hz	88Hz	28Hz
16	single	35Hz	32Hz	28Hz	17Hz
	multiple	53Hz	47Hz	39Hz	20Hz

The standard deviation of the sensors used on the sensor strip are shown in Figure 3.13. The results are in agreement with those shown in Table 3.2. Albeit that the spread of the 128 internal averaging is smaller then that of 512 internal averaging, the reason for this could be that the sensor strip was not placed in the film canister but rather in an sealed bag. The bag is more sensitive to external influences and because the 512 averaging mode takes the longest to run it is also the most susceptible.

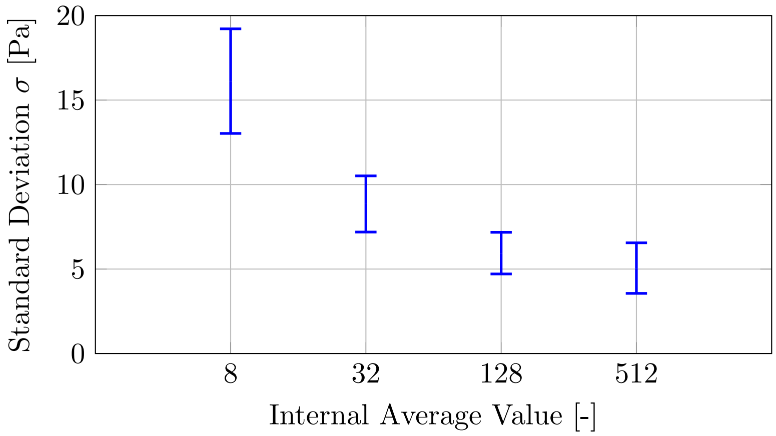

Figure 3.13: Standard deviation range for the different internal averages values of pressure strip 1.

Chapter 4

Free Stream Parameters

As previously mentioned in Chapter 3, in order to define the pressure coefficients, one requires additional free stream values for dynamic and static pressures (see Equation 3.1). A method or unit to measure these values is favorable as it will fly with the kite, therefore maintaining a compact and lightweight system is required. Because the dynamic pressure is related to the velocity through Bernoulli's equation:

$$q = p_0 - p_s = \frac{1}{2}\rho V^2 \tag{4.1}$$

Either quantity can be measured. An additional requirement was to integrate the dynamic or velocity measuring system in the kite control system, which is in contrast to the pressure measurement strip which was built as a standalone system. The reason for the integration is that the measured or computed velocity from such a system is the apparent wind velocity of the kite. This is an important parameter to estimate the performance of the kite, and there are future plans within the group to incorporate this parameter in the kite controller. Therefore the logging has to be performed within that system.

This gives a range of options such as mechanical anemometer, sonic anemometer ,and pitot-static tubes. The static pressure requires the presence of a static port or measurements on the ground which are then corrected for altitude and atmospheric conditions. The one system that combines both measurements is the pitot-static tube. Previous work done within the KitePower group also resulted in the implementation of a pitot-static tube however the sensor specifications were unknown and the system was never calibrated. The previous system however did solve the problem regarding the constant changing angle of attack and side slip angle. The pitot-static tube was employed within a gimbal and used a badminton shuttle for the weathercock effect. Both the gimbal and the badminton shuttle were employed in the new system.

This chapter will deal with the sensor selection, pitot-static tube analysis and system calibration. In the final section data from one flight test performed with the new pitot-static system will be discussed.

4.1 Sensor Selection

There are two types of pressure sensors available for the pitot-static tube, a differential pressure sensor or a combination of two barometric pressure sensors. The second option seems less practical as it would require measuring two large values (10^5) and subtracting them to obtain a value of lower significance. However, one possibility is the combination of two LPS25H which were previously tested. The selection of an appropriate sensor was based on the following three criteria:

Size and weight due to the airborne nature of the system and its suspension between the bridles.

Operational range within the expected kite flight envelope. An analysis of the performance of the two kites currently used, the V3 and the Genetrix Hydra, resulted in an expected apparent wind velocity for the Hydra of around 27ms^{-1} and for the V3 around 20ms^{-1}[49].

Accuracy reproducibility and small spread of data.

A list of possible differential pressure sensors is given in Table 4.1. Note that large and heavy sensors (> 50g) were omitted from the list even though they have accuracies in the range of 0.01%.

Table 4.1: Different differential pressure sensors considered for pitot-static system.

Brand	Model	Range [Pa]	Accuracy		Weight [g]
			% Full scale (F.S.)	% Measured value (m.v.)	
Honeywell	142PC01D	6895	1.05	0	
Kavlico	P993	1250	2	0	
Sensirion	SDP1000R	3500	0.4	2	14
	SDP2000L	3500	0.2	2	14
Sensor Technics	LBA series	500	1.5	1.5	
Measurement Specialist	MS4525	6895	1	0	3

The accuracy of the sensors given in Table 4.1 are compared by computing the velocity uncertainty for each sensor in the kite flight envelope. The velocity uncertainty is computed with the following equation:

$$V_{\text{unc}} = V(q_{\text{sensor}+}) - V(q_{\text{sensor}-}) \tag{4.2}$$

where $V(q_{\text{sensor}+})$ and $V(q_{\text{sensor}-})$ are the velocities computed at the worst maximum and minimum dynamic pressure error cases defined as:

$$q_{\text{sensor}} = q_{\text{real}} \pm (q_{\text{real}} \cdot \delta_{m.v.} + p_{\text{F.S.}} \cdot \delta_{\text{F.S.}}) \tag{4.3}$$

δ is the given error for that sensor in Table 4.1. Subscript real is for the actual value that should be read by a sensor, if it were to have zero errors. The dynamic pressure is converted to velocity with the following equation:

$$V(q) = \sqrt{\frac{q}{\frac{1}{2}\rho_{\mathrm{ISA}}}} \tag{4.4}$$

The density ρ is taken at standard atmosphere and is equal to $1.225\mathrm{kgm}^{-3}$. The velocity uncertainty for sensors given in Table 4.1 are illustrated in Figure 4.1.

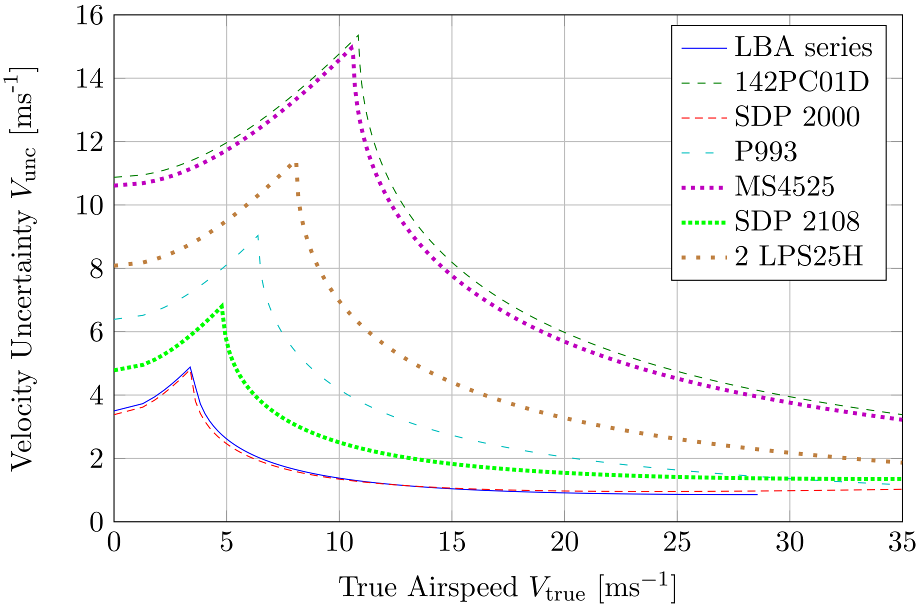

Figure 4.1: Comparison of the different sensors error on the indicated velocity.

From the figure it can be seen that the sensors that have an error that is measured value depended have the lowest error in the low speed regimes. The kink displayed by all the sensors is due to the omittance of negative dynamic pressures which are defined as zero. The two sensors with least amount of error are the SDP2000 by Sensirion and the LBA Series by Sensor Technics. The LBA Series has lower error above $15\mathrm{ms}^{-1}$ than the SDP2000, but its operational range is up to $27\mathrm{ms}^{-1}$. This limit is equal to the expected velocity limit for the Genetrix Hydra kite, so in order to account for both wind gusts and inaccuracies of the expected velocities it is chosen to use the SDP2000 sensor.

The SDP series sensors do not have the traditional mechanical membrane as their sensing mechanism. The sensors employ a different technology that is based on CMOS technology, it can be compared to the hot-wire anemometer. By allowing a small flow through the sensor a heating element heats the air and this is sensed by the CMOS chip and converted to a pressure difference by internal electronics.

In order to incorporate this sensor into the kite system additional components were required. The sensor interface was selected to be analog and the sensor requires a supply

Figure 4.2: SDP1108 sensor by Sensirion non linear version of the SDP2000 differential pressure sensor using same package[50].

of 5V. The output of the sensors ranges from 0.25V to 4.00V, giving it an output span of 3.75V. The analog output is converted to pascals with the following equation,

$$p = \frac{U \cdot 3500}{3.75} \tag{4.5}$$

In order for the sensor to function properly the supply voltage has to be kept at a constant 5V, therefore a high precision voltage reference is used (LT1416CCS8-5.0 by Linear Technology). The reference converts the 11.1V supplied by the pod to 5V at close proximity to the sensor, therefore it is mounted on a small PCB for which the schematic drawing is given in Figure B.4.

Because a differential sensor was selected an additional sensor is required, the reason being that the static pressure is needed explicitly to compute the pressure distribution over the wing according to Equation 3.1. Not wanting to measure the static pressure on the ground and correcting for altitude afterwards, it was opted to include an LPS25H sensor to the pitot-static system. By placing the LPS25H sensor in the film canister it can be connected to the pitot-static tube using a T-connector. The current Electrum-100 board on which the KCU operates there is a conflict with the I^2C driver, therefore a USB-ISS adapter is used to give the Electrum-100 I^2C capabilities. The USB-ISS is a plug and play USb adapter that gives I^2C capabilities to any device and is shown in Appendix Figure B.5. Additionally the LPS25H will be functioning at a long distance from the KCU, it will therefore require additional electronics to communicate over I^2C at large distances. A buffer bus based on the P82B96TD by NXP was made between the KCU and pitot-static unit. Both local I^2C operate on 3.3V, this is standard for the USB-ISS adapter while at the pitot-static system a 3.3V voltage reference (LT1416CCS8-3.3 by Linear Technology) is used on the available 11.1V present. The buffer bus on the other hand runs on 11.1V. The components near the pitot-static system are mounted on the same PCB as the 5V reference and the circuit diagram can be seen in Appendix Figure B.4, while the buffer adapter in the KCU is connected to the USB-ISS buffer according to the scheme shown in Appendix Figure B.6.

4.2 Pitot-static Tube and Gimbal

There are numerous options when selecting a suitable pitot-static tube for the kite system. However, the cost and robustness are important factors that were taken into account. A survey performed on possible velocity measurement systems within the group has indicated that the cost of high quality pitot-static tubes is around a thousand euro per unit[51]. This price tag is considered too high for the current state of the KitePower system. Multiple tubes will be required due possible damage to the pitot-static tube during launching and landing, crashes or while handling the system. Therefore, it was opted to use a pitot-static tube by SM-Modellbau which was originally intended for use in model airplanes. These pitot-static tubes have a unit cost of around 20 euros, a specimen is shown in Figure 4.3.

Figure 4.3: Pitot-static tube by SM-Modellbau used in the kite system.

The performance of a pitot-static tube depends on the following three parameters:

- Tip shape
- Distance between the static holes and stem (A)
- Distance between the tip and static holes (B)

The distances are generally normalized with respect to the tube diameter. These are indicated in Figure 4.4 while Table 4.2 defines these for the SM-Modellbau pitot-static tube. The stem to static holes distance is not defined for the current system as it does not have a stem but it will incorporate the badminton shuttle, the given A is defined as the distance from static holes to hose connectors. To successfully mount the pitot-static tube and badminton shuttle on the gimbal, the pitot-static tube is inserted into a carbon rod that goes through the badminton shuttle tip.

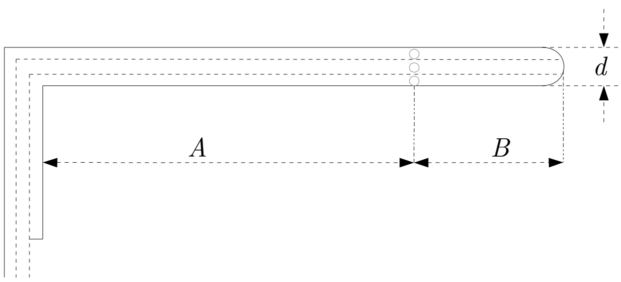

Figure 4.4: Schematic representation of a Prandtl pitot-static tube.

Table 4.2: Specifications of the pitot-static tube by SM-Modellbau.

		x/d
d	4.00mm	1
A	56.75mm	14.2
B	5.25mm	1.3

While all three parameters influence the static pressure, the total pressure is only affected by the tip shape. The tip shape determines the angle of attack range for which acceptable

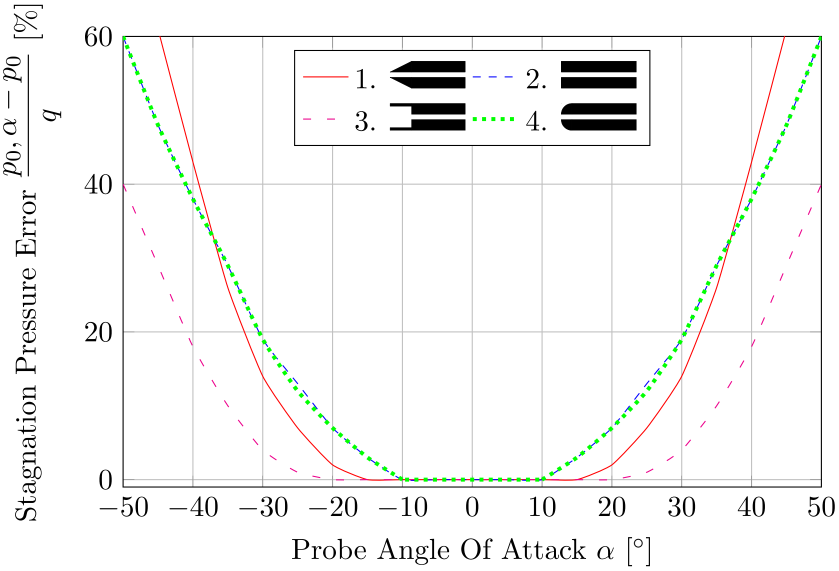

Figure 4.5: Angle of attack influence on stagnation pressure of different pitot heads[52].

total pressures are obtained. The error induced for four different tip shapes for a range of angles of attack is given in Figure 4.5. The pitot-static tube by SM-Modellbau has a spherical tip similar to number 4 in Figure 4.5, which gives a range of ten degrees in any direction with little to no influence in the read total pressure. In fact all four examples given have at least ten degrees angle of attack range with an error of zero. Such a standard graph for the static pressure error is not as straightforward, because the static pressure is also influenced by the distance between tip and stem. The error induced at zero angel of attack for a spherical tip is shown in Figure 4.6. The difference between the standard and

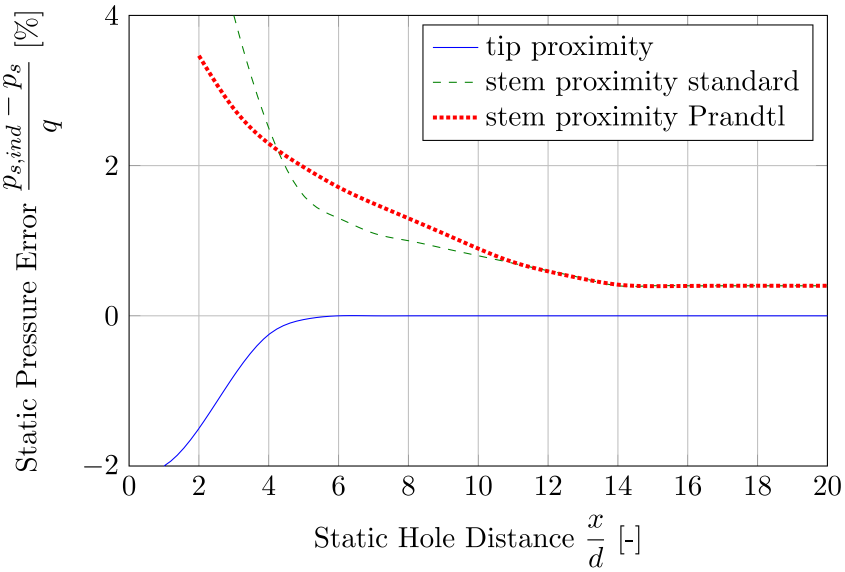

Figure 4.6: Static tube error estimation curves[52].

Prandtl stem is the shape of the joint between the tube and stem, which in the case of the Prandtl is a 90 degree corner (See Figure 4.4) and the standard has a curved joint with a radius of approximately three times the tube diameter. For the current pitot-static tube only due to tip disturbance the sensed static pressure will be about 1.8% too low. But because the current system includes a badminton shuttle for flow alignment the influence on the static pressure is outside the range of this figure. For the errors in the figure it is given that the stem has equal diameter to the tube while for the current system the badminton shuttle has a tip diameter of 26.7mm and an aft diameter of 70mm compared to the tube diameter of 4mm. The effect of the shuttle on the sensed static pressure will be analyzed in Section 4.3.

Regarding the gimbal previous work indicated stable behavior of the system. In addition to the range of angles of attack at which the total pressure can be sensed accurately, this gives some leeway in the behavior and alignment of the system, even though the effects on the static pressure measurements are unknown.

In order to quantify and calibrate the pitot-static system, the components will be tested in the wind tunnel. The gimbal construction including badminton shuttle and pitot-static tube is shown in Figure 4.7 during the wind tunnel calibration tests which will be explained in the next section.

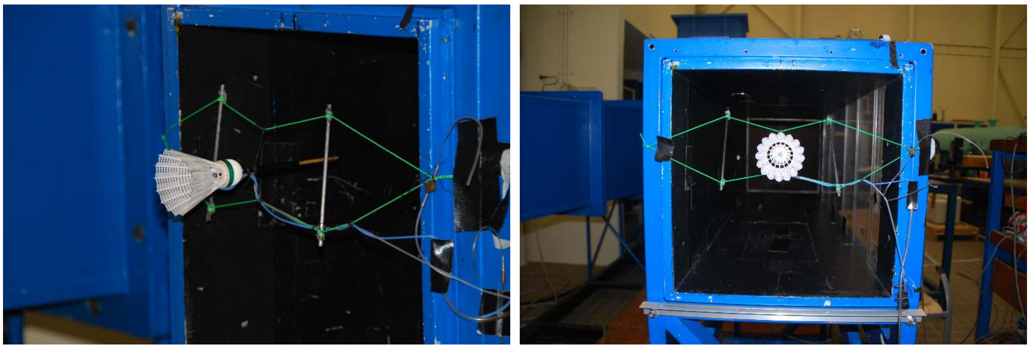

(a) Side view *(b) Rear view.*

Figure 4.7: Pitot-static system including gimbal, during wind tunnel calibration.

4.3 Wind Tunnel Calibration

The wind tunnel calibration was necessary to generate a calibration curve, which is a correction on the measured value with respect to the true value. This calibration curve has to account for all the errors in the system. As already mentioned in the previous sections there are three points where an error is introduced in the system:

- Sensed total pressure
- Sensed static pressure
- Sensor error

These wind tunnel tests were performed in the M-tunnel which was described in Section 3.2.

4.3.1 Total Pressure

This test was used to analyze the total pressure sensed by the kite pitot tube. The pitot-static tube including gimbal is mounted in the wind tunnel as shown in Figure 4.7. A schematic drawing of the connectors and sensors used for this is given in Figure 4.8.

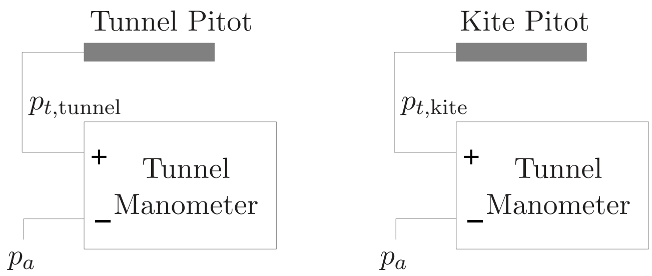

Figure 4.8: Total pressure measurement setup.

The result of these measurements is given in Figure 4.9. The result can be split into two regions, the measurements below 50Pa and those above. For the measurements performed at more than 50Pa the total pressure error lower than 1%. For the measurements below 50Pa larger errors are found. The reason for this is that the weather cock effect that should be induced by the badminton shuttle does not have enough force to overcome gravity and thus the pitot-static tube points downwards. So by comparing these results with Figure 4.5, one can say that the pitot-static tube is aligned with the flow within $\pm 10°$ for values above 50Pa, and for lower values the miss alignment angle is larger. Estimated for 6% error is a miss alignment of around 15-20 degrees according to Figure 4.5.

4.3.2 Static Pressure

The static pressure error consists of the following two phenomena, the flow acceleration over the tip which results in a lower static pressure and the flow stagnation at the stem which results in an increased static pressure. For the current system it is difficult to measure or define these two parts of the static pressure error separately, therefore the error was measured a single value. For this experiment the pitot-static tube and badminton shuttle were removed from the gimbal and mounted on a long rod. The rod was positioned in the center of the wind tunnel test section. Additionally an extra static tube was used and is referred to as the reference static pressure. The dimensions of the reference static tube are given in Table 4.3. The reference pitot tube was placed in the same location as the kite pitot-static tube.

The error was measured for the kite pitot-static tube with different badminton shuttle distance (defined as A+B in Figure 4.4) and without the shuttle. The reference static tube

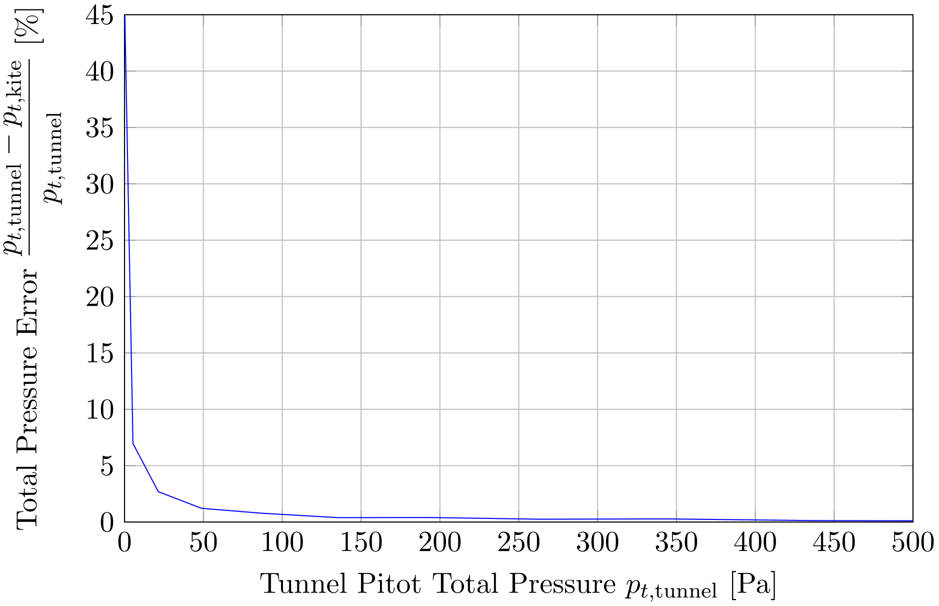

Figure 4.9: Total pressure error of kite pitot-static tube mounted on the gimbal.

Table 4.3: Specifications of the reference static tube used in the wind tunnel.

		x/d
d	0.90mm	1
A	25.00mm	27.8
B	4mm	4.4

error was measured without the badminton shuttle. The results of these measurements are given in Figure 4.10.

When the results are compared to the error prescribed by Figure 4.6 it is noticeable that only the reference static tube displays a somewhat constant error. If the error for the reference static tube is computed with the dimensions in Table 4.3 and the model of Figure 4.6 this yields an error of +0.5% which compared to the measurement results that vary from 0.9% to 0.4% there is some agreement. In the case of the kite pitot-static tube alone without the badminton shuttle, the error is not constant, although it flattens at the higher values of the dynamic pressure. The negative error in the static pressure is caused by the tip presence, because the magnitude is larger than what was predicted by Figure 4.6 can indicate a few things such as:

- The errors computed with Figure 4.6 do not hold for "thick" tubes.
- The tip of the pitot-static tube is actually not spherical.
- The surface of the pitot-static tube is not smooth.
- The shape and size of the static ports are not optimal.

When the badminton shuttle is combined with the pitot-static tube it adds a positive error and there by making the total error less negative. This is in agreement with the

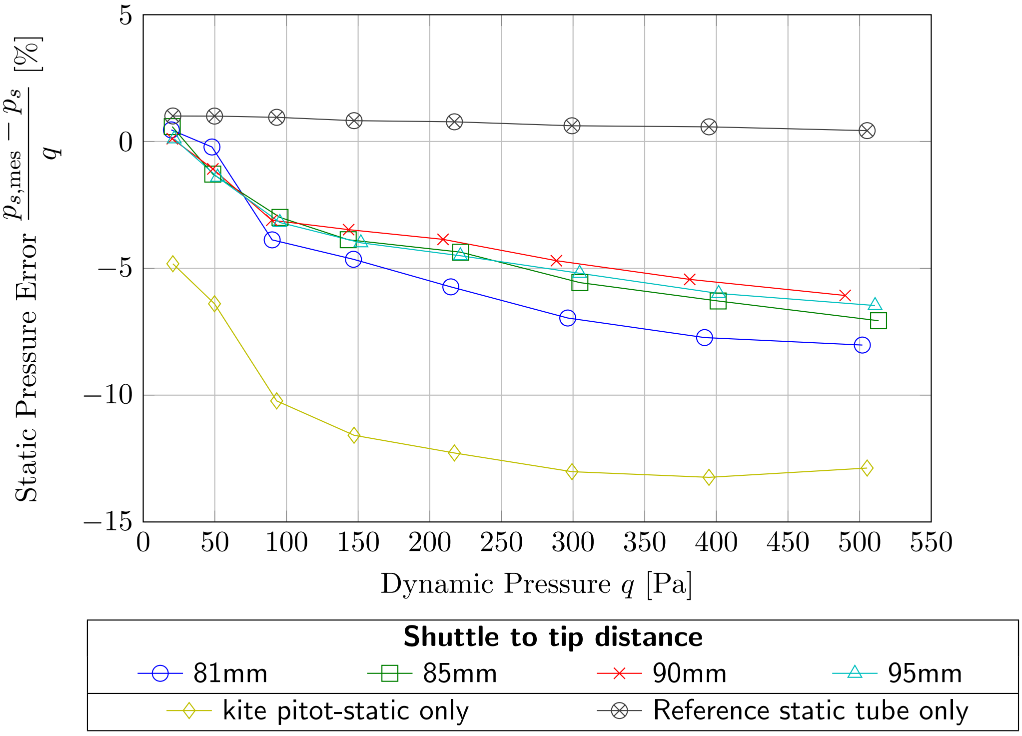

Figure 4.10: Static pressure error with varying badminton shuttle location distance.

presence of the stem that also introduces a positive error. The trend of the curves are similar to that of the shuttle-less tube, but the flattening at high dynamic pressures is less clear. The overall least amount of error is found for a pitot-static tip to badminton shuttle distance of around 90mm.

4.3.3 Differential Pressure Sensor

The fact that the chosen sensor functions by allowing a small amount of airflow through it also introduces errors when hoses are combined. The diameter of the hoses has a inverse effect on the error, small diameters incur large errors. This property was not known during the selection of the sensor but was rather stumbled upon during the wind tunnel tests. While the kite pitot-static tube has 1mm internal diameter hoses, the wind tunnel pitot has hoses with a 3mm internal diameter.

4.3.4 Full Pitot-static System Calibration

The results of the static pressure error of the pitot-static tube by SM-Modellau has shown the quality is not desirable. However, at the moment there were no other pitot-static tubes available for its implementation in the kite system. In addition to this the error introduced by the working principle of the differential pressure sensor (SDP2000) cannot be measured separately. The pitot-static system was calibrated while in in-flight configuration. This configuration includes the gimble, pitot-static tube, badminton shuttle, differential pressure sensor SDP2000 and the LPS25H MEMS barometric pressure sensor in film canister. For this configuration the pitot-static tip to badminton shuttle distance is 108mm. A schematic representation of the experiment setup is given in Figure 4.11.

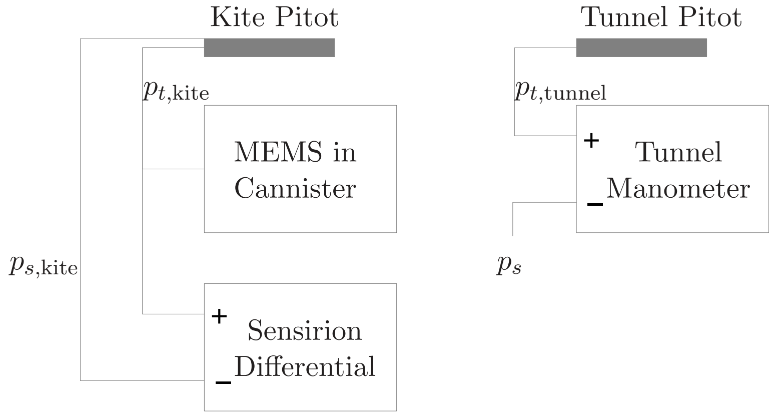

Figure 4.11: Pitot calibration tunnel setup.

During the calibration experiment the wind tunnel is operated at different speeds while the real dynamic pressure is measured by the tunnel manometer and the indicated dynamic pressure is given by the SDP2000. A linear fit is through the points of this measurement to create a 1$^{\text{st}}$ degree polynomial that gives the calibrated dynamic pressure per sensor, for sensor #1 the polynomial is as follows,

$$q_{\text{cal}} = 1.29 q_{\text{ind}} + 0.37 \tag{4.6}$$

and for sensor #2,

$$q_{\text{cal}} = 1.32 q_{\text{ind}} + 1.22 \tag{4.7}$$

The error between the calibrated dynamic pressure and real dynamic pressure is given in Figure 4.12.

As can be seen from Figure 4.12 the errors for indicated dynamic pressures higher then 50Pa are less then $\pm 1\%$ for both sensors. At values below 50Pa for the indicated dynamic pressure there are larger errors. The reason for larger errors at lower values of the indicated dynamic pressures can be attributed to the lower accuracy of the SDP2000 at lower range and miss alignment of the pitot-static tube with the incoming flow. As one can recall during the analysis of the total pressure error of the pitot-static and gimbal in Figure 4.9, for lower pressures there is a miss alignment to which the static pressure is even more sensitive to. This could result in additional errors in the lower regions and different shape of the plot that does not match the linear fit properly.

MEMS Static Pressure Measurement

The MEMS sensor is intended to measure the static pressure, however due to the deviation from ideal situation caused by the working principle of the differential sensor it is chosen to place the MEMS sensor on the total pressure line. This is because the small amount of flow would result in a indicated static pressure that differs from the real static

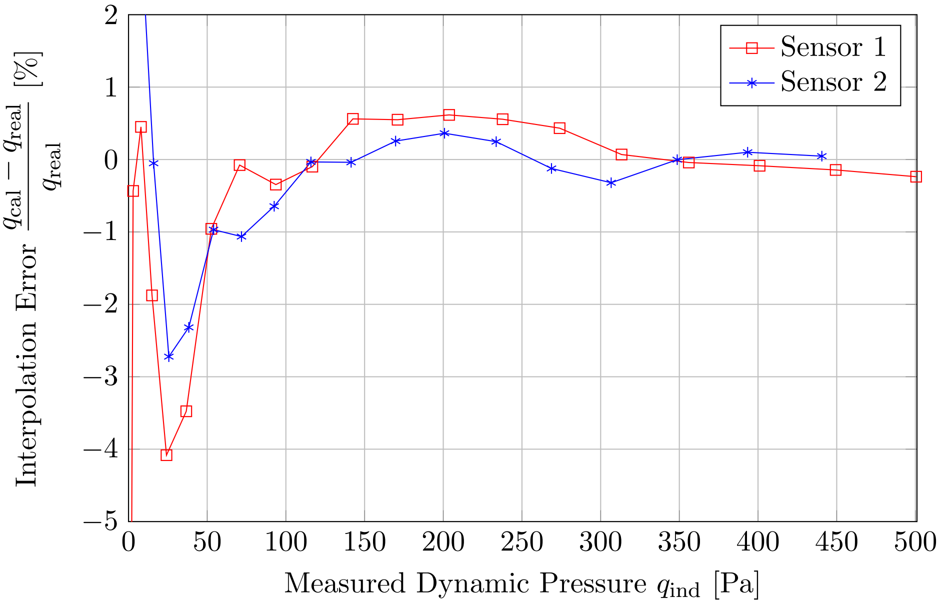

Figure 4.12: Error between the interpolation and the measured values.

pressure, thus requiring calibration. As was shown during the selection and validation of the LPS25H sensor (Section 3.3) that the its error is not measurement dependent, and therefore the measurement of a higher pressure (total pressure) is better than measuring a lower pressure (static pressure). In order to convert the indicated total pressure to the static pressure the pressure change indicated and is defined as the dynamic pressure based on the ambient pressure.

$$\Delta p_{\text{MEMS}} = p_t - p_a \tag{4.8}$$

As a open wind jet wind tunnel is used and no lifting body is present it can be assumed that the ambient pressure is equal to the dynamic pressure. The static pressure can therefore be computed with the following

$$p_{\text{s}} = p_{t,\text{ind}} + p_{\text{offset}} - \Delta p_{\text{MEMS}}(q_{\text{ind}}) \tag{4.9}$$

In the previously stated equation the pressure offset p_{offset} is a linear offset in the sensor that occurs due to manufacturing and assembly of the LPS25H on a PCB. The offset for pressure sensors 1 and 2 are -1328Pa and -696Pa. The indicated pressure change is calibrated with respect to the indicated dynamic pressure. In the ideal situation the calibration should be one to one. By fitting a 1^{st} degree polynomial through the measured data $\Delta p_{\text{MEMS}}(q_{\text{ind}})$ is found to be

$$\Delta p_{\text{MEMS}} = 1.1 q_{\text{ind}} + 2.1 \tag{4.10}$$

for MEMS sensor # 1 and,

$$\Delta p_{\text{MEMS}} = q_{\text{ind}} + 9.3 \tag{4.11}$$

is found for MEMS #2. The one to one fit is found for sensor 2 however this is not the case with sensor 1. A cause of this can be that the sensors used are still the prototype, improper closure of the film canister, differential pressure sensors errors and inaccuracies, or the fact that during this experiment the Snowball was malfunctioning and thus the data was logged with a read out device supplied by the manufacturer. The settings of the read out device could not be changed nor checked for internal averaging mode. The errors for the interpolations are illustrated in Figure 4.13.

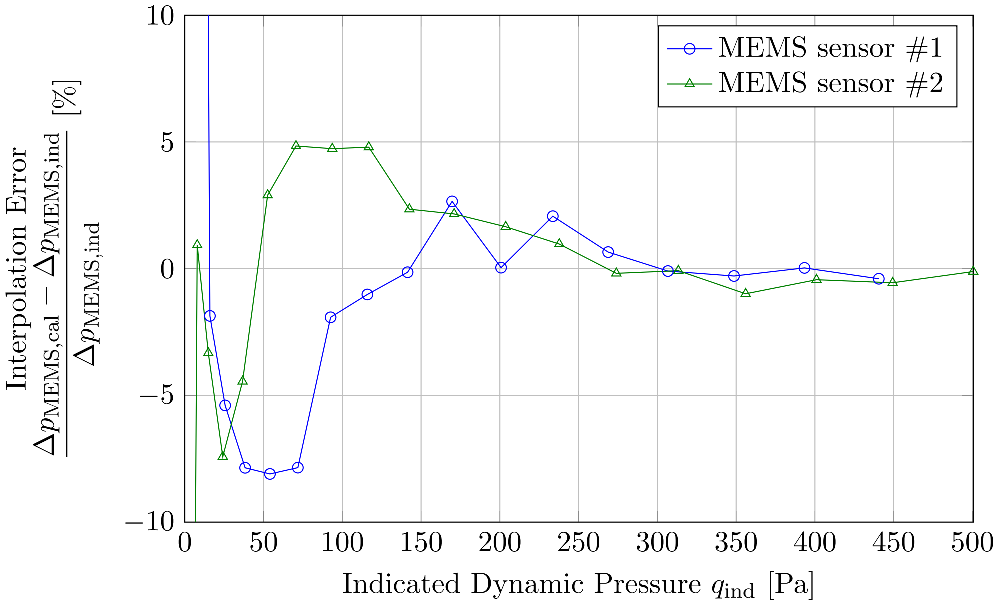

Figure 4.13: Fitting error for the static pressure measurement with the MEMES sensors.

For the results of the interpolation errors, the error at the lower range of the measurements is higher than those above an indicated dynamic pressure of about 150Pa. This is in agreement with the device property, that its error is not measured value dependent.

4.4 Flight Data

The pitot-static tube system was flown once only before the writing of this thesis. The data set for this flight test is very short as only three complete figures of eight were achieved before tether rupture suspended all further testing. Besides this the MEMS LPS25H sensor stopped functioning before the kite system was airborne so no data from this sensor was logged. The only available data is from the differential pressure sensor #1. The measured signal is converted from voltage to the dynamic pressure with Equations (4.5) and (4.6). With the computed dynamic pressure the apparent wind velocity of the kite can be found with the following:

$$V_a = \sqrt{\frac{2q}{\rho}} \tag{4.12}$$

In here ρ is the actual density at the test location, by using the ideal gas law the density follows from:

$$\rho = \rho_{\mathrm{ISA}} \frac{p}{p_{\mathrm{ISA}}} \frac{T_{\mathrm{ISA}}}{T} \tag{4.13}$$

The values for international standard atmosphere density, pressure, and temperature are 1.225kgm^{-3}, 101,325Pa, and 288.15K. As was mentioned before the MEMS pressure sensors was not functioning, thus both the temperature and the pressure during the flight test are taken from the Royal Netherlands Meteorological Institute (KNMI) weather data base as the day average[53]. The values found for the average on the flight day are 289.45K for the temperature and 101,550Pa for the pressure.

One figure eight maneuver is extracted from the flight data. The position of the kite with respect to the angles and the corresponding time stamp for the selected figure eight maneuver is shown in Figure 4.14.

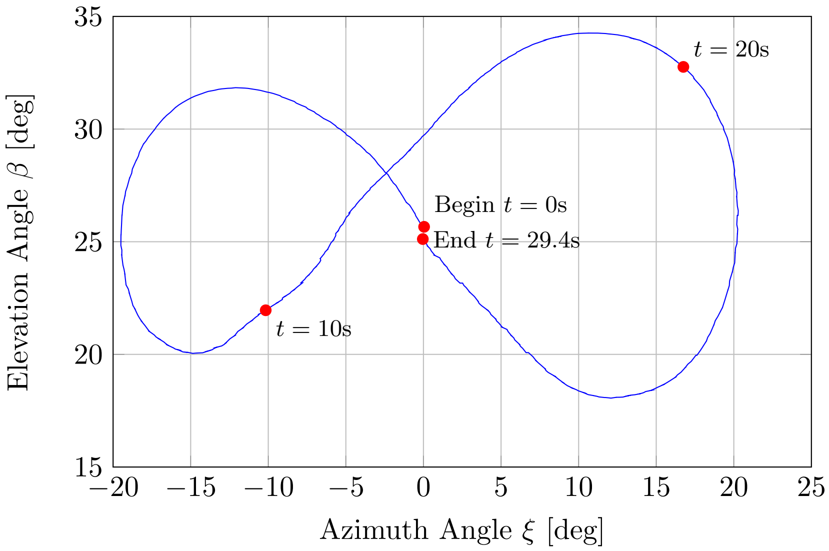

Figure 4.14: Kite position during the figure eight maneuver.

Because the force is related the square of the velocity Figure 4.15 shows the square root of the force and the apparent wind velocity.

Noticeable from Figure 4.15 is that most of the peaks and valleys coincide or are slightly shifted. The inconsistency of the aerodynamic forces on the kite is observed due to the changes in the either graph are not inversely proportional. This would then require the force coefficient of the kite to change. The measured apparent wind velocity can also be compared to the steering input, as large steering inputs cause deformations in the kite (twist) which increases the drag[7]. The increased drag should translate to a reduced velocity. In Figure 4.16 the data from the steering encoder[1] is plotted with the apparent wind velocity for the same figure eight maneuver as before. A steering input of zero means both steering lines are of equal length while a positive value indicates a right steering input and negative value a left steering input. The biggest peaks and valleys of the apparent wind velocity coincide with a steering input, especially the slowest velocity

[1]The encoder is connected to the steering mechanism through a gearbox, so one encoder rotation is about six rotations of the steering tape wheel.

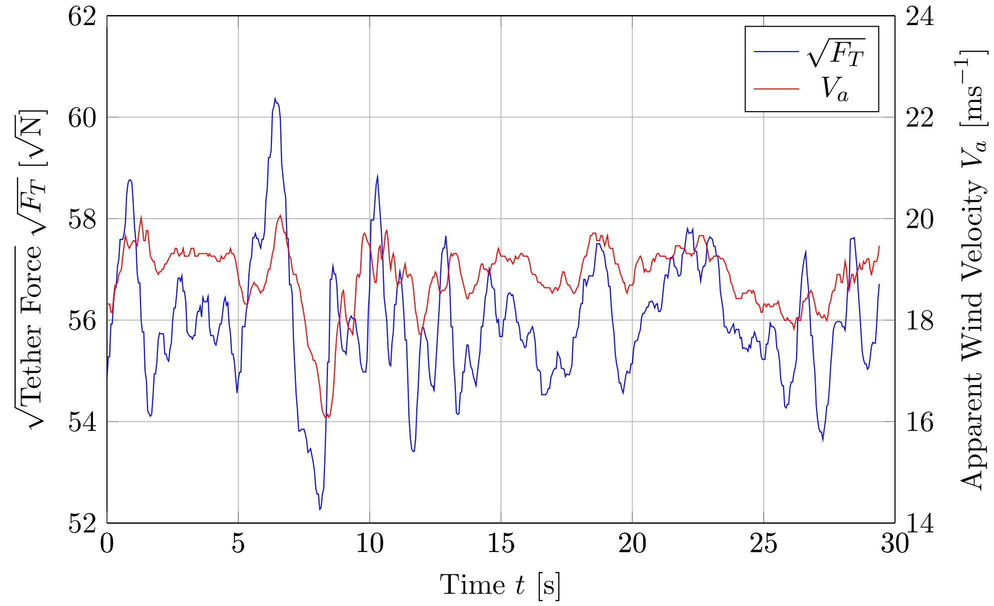

Figure 4.15: Comparison of the apparent wind velocity and tether force during a figure eight maneuver.

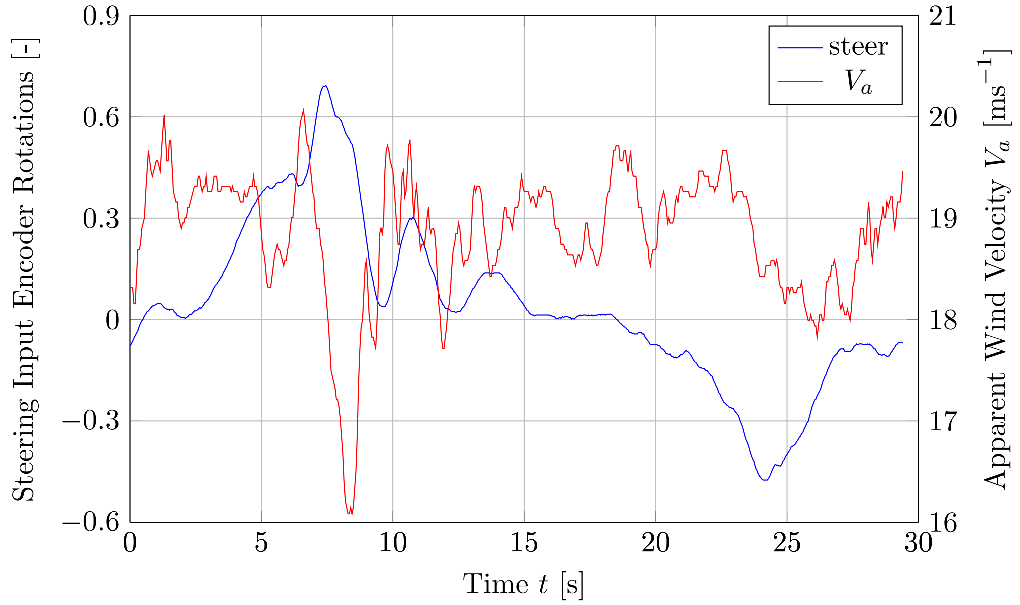

Figure 4.16: Steering input with respect to neutral compared to the apparent wind velocity during a figure eight maneuver.

which directly follows the biggest steering input. This shows that the pitot-static system is able to detected the changes in the apparent wind velocity caused by the increased drag of the steering inputs.

Chapter 5

Wind Tunnel Validation

Before the MEMS pressure distribution strip can be placed on a kite it needs to be validated on a known wing section. This chapter will discuss the test setup, procedure and results of the MEMS sensor strip validation.

5.1 Test Setup

Most of the equipment used in this test set have been described in Section 3.2, these are the wind tunnel, sensors data acquisition and tunnel manometers. In addition to these there is the wing profile on which the sensors will be tested. The NACA-64418 has built-in pressure tabs which were used to compare the results of the MEMS pressure strip. The wing section is mounted vertically in the M-tunnel as shown in Figure 5.1.

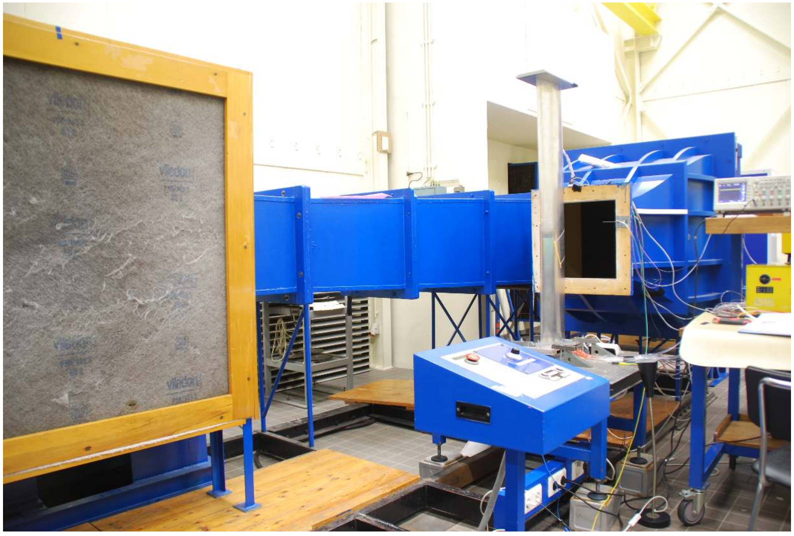

Figure 5.1: The NACA-64418 wing section placed vertically in the M-tunnel.

The wing section is leveled horizontally so that no sweep is introduced. The wing section is centered in the test section such that the pressure tabs are in the lower half of it, while allowing free space in the upper half to place the pressure strip. Alignment of the wing section with respect to the flow was done by naked eye, the reason for this being that the jig required for angle of attack alignment for this wing section was not available. Although, this could cause problems if the results would be compared to computational models. However, this validation test is a one to one comparison of the pressure tabs and the MEMS sensor strip. Each pressure tab in the system is connected to a hose that needs to be connected to a manometer, to achieve this a manual scanivalve is used. This then requires a single manometer, both the scanivalve and the manometer are shown in Figure 5.2. As the MEMS pressure strip will be only tested on the upper surface of the wing section, only half of the pressure tabs are used. The hoses coming from the are shown in Figure 5.3.

Figure 5.2: Manual scanivalve and DPG2400 mensor used.

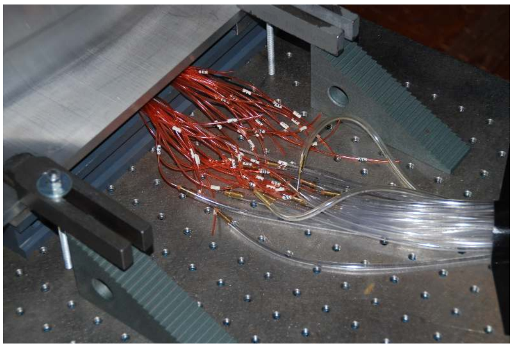

Figure 5.3: Hoses coming from the pressure tabs (red) and going to the scanivalve (clear).

Although a pitot-static tube was designed and calibrated for the kite system, this will not be used during the wind tunnel validation. The main reason for this is the lack of a suitable mounting location as the whole gimbal and badminton shuttle should be deployed. Additionally, the wind tunnel already features a pitot-static tube. The pitot-static tube was also connected through the scanivalve to the manometer, with the static line functioning as the reference pressure for all measurements.

The MEMS pressure strip is mounted on the wing surface using double sided tape. The sensors are aligned parallel to the incoming flow.

5.2 Test Procedure

A baseline measurement is made on a clean profile using the pressure tabs. Due to the laminar flow properties of the NACA-64418 a trip strip is placed to force the boundary layer to transition from laminar to turbulent. As the pressure sensors are 1mm high, different trip strip thicknesses were used ranging from 0.25mm to 0.85mm and were placed at approximately 3-5% of the chord. The results of the reference run are found in Figure 5.4. This reference data will be used as the baseline for comparison with the MEMS pressure distribution results according to the trip strip employed in that test.

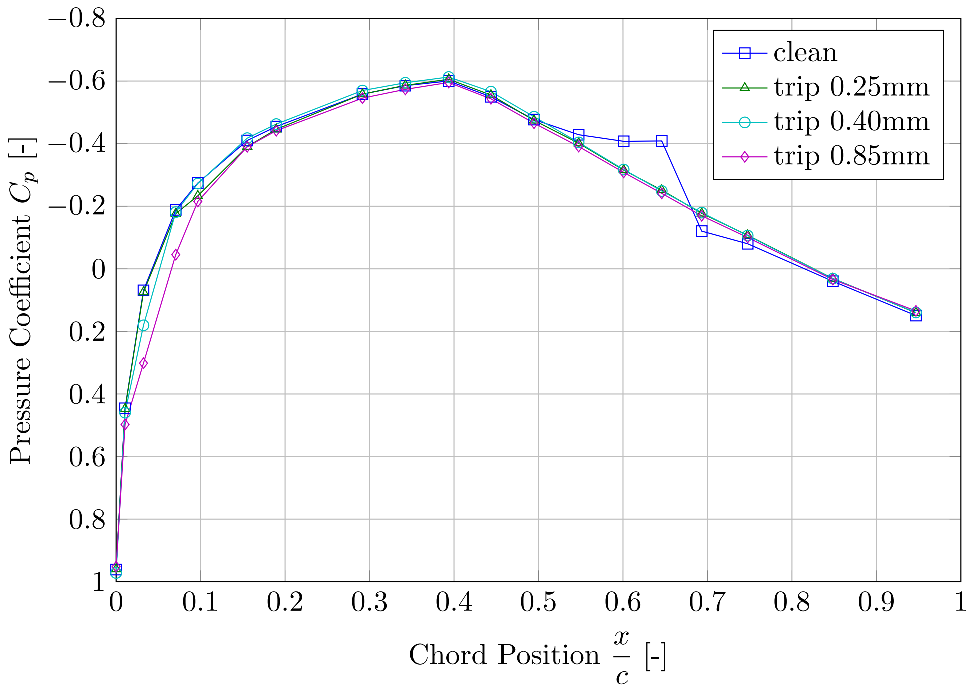

Figure 5.4: Pressure distribution on the upper surface of the NACA-64418 measured through surfaces tabs.

The laminar separation bubble is clearly visible for the clean configuration at about 0.7 chord, while it is not present for the other three cases where the flow is tripped. Also noticeable is the influence on the pressure tabs directly behind the trip strip. The flow needs certain distance to transition and the thicker the trip strip thus the larger this transition distance.

With regard to the pressure distribution measured with the MEMS pressure sensors, the reference pressure is measured before and after the wind tunnel operation and is equal to the ambient pressure. To ensure that this reference pressure is valid the static pressure of the wind tunnel in operation was compared to the ambient pressure, the difference did not exceed 4Pa on measurements performed at a dynamic pressure of 500Pa, which is the dynamic pressure during all wind tunnel tests unless otherwise specified. The difference of the static and ambient pressure is less than 1% and therefore neglected during the experiments.

5.3 Results

There was initially no agreement between reference pressure tab measurements and the MEMS pressure strip. It is suspected that the cause of this disagreement could be the shed vortices from the sensor upstream interacting with those downstream. In order to try to eliminate this interaction the sensor strip was placed skewed on the wing section surface as indicated in Figure 5.5.

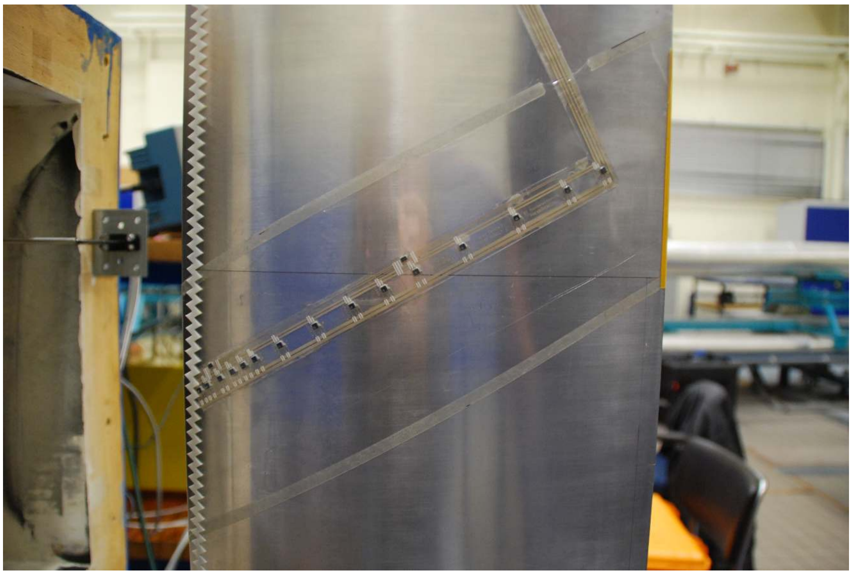

Figure 5.5: The MEMS pressure strip mounted skewed on the profile, the straight line on the profile is the straight position reference.

The resulting pressure distributions for the straight and skewed positioning of the sensor strip on the wing section with the 0.85mm trip strip are given in Figure 5.6.

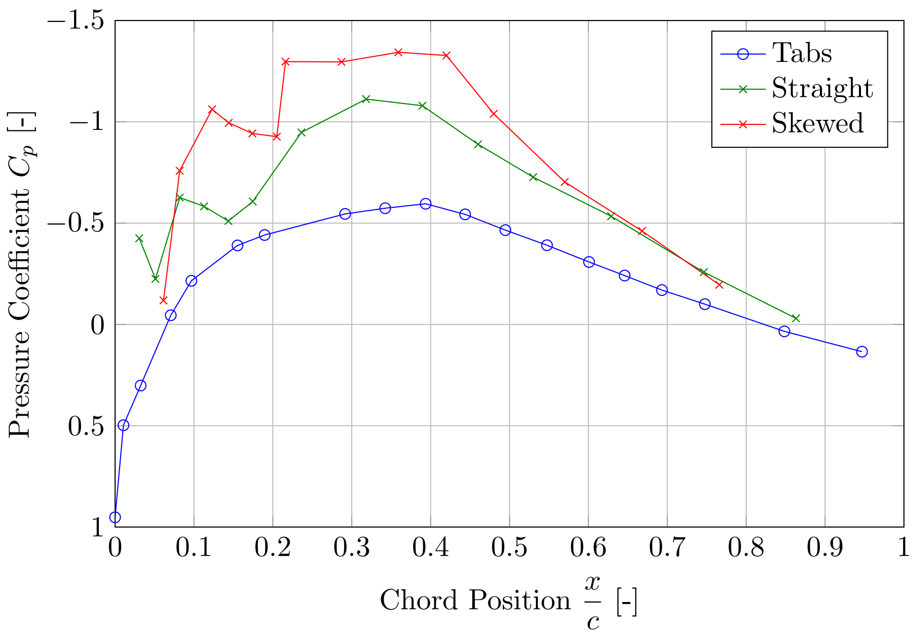

Figure 5.6: Comparison of pressure distribution measured with pressure tabs and MEMS pressure strip both straight and skewed, including trip strip of 0.85mm at 3-5% chord.

From Figure 5.6 it is clear that the skewed orientation is even worse than the straight one. Although, some trend is seen that follows the shape of the reference pressure. It should be noted that during placement and removal of the strip on the wing section two sensors became damaged. One due to the high curvature of the nose of the profile which it was not able to achieve and became undone from the PCB. The second sensor got dislodged while peeling off the strip, a kink formed in the PCB due to stronger than expected bonding of the tape. Because of the discrepancies between the MEMS pressure sensors and the pressure tabs some improvements and modifications were introduced.

5.3.1 Improvements

From literature it can be found that bodies and elements are used to create so-called frustum to achieve smooth transition to the sensing hole[34]. A smooth transition is better than the abrupt step increase caused by the plain sensor. In order to achieve a smoother transition cellophane is used. By covering a large area surrounding the sensor strip with cellophane and tightening it by blowing hot air on it, creates a smoother surface transition. To minimize the displacement of the strip it is first applied to the skewed sensor positioning. Because the cellophane covers the sensing hole of each sensor these had to be cut out individually after the cellophane was tightened. Figure 5.7 shows a closeup of a sensor covered by cellophane and the cutout made for the sensing ports unfortunately the cellophane used was clear and not really visible but the white edges of the cutout are.

Figure 5.7: Closeup of the cutout made in the cellophane at a sensor sensing port.

The results of the skewed placed sensors with the addition of the cellophane are given in Figure 5.8.

There is an improvement in the results compared to the initial setup. The difference between the tabs and the MEMS pressure distribution is smaller, however it still is around 30% at minimum C_p. Also noticeable is that the different configurations of the MEMS pressure strips are more or less equal. However the improvements are still not sufficient, therefore the sensor strip is placed parallel to the incoming flow because the result of the

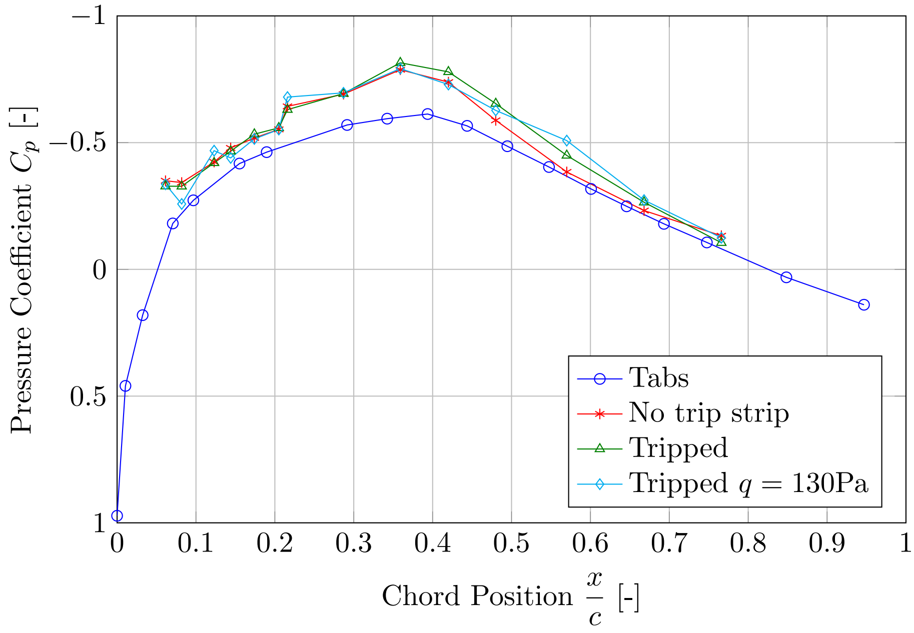

Figure 5.8: Comparison of pressure distribution measured with pressure tabs and skewed MEMS pressure strip covered by cellophane, including trip strip of 0.40mm at 3-5% chord.

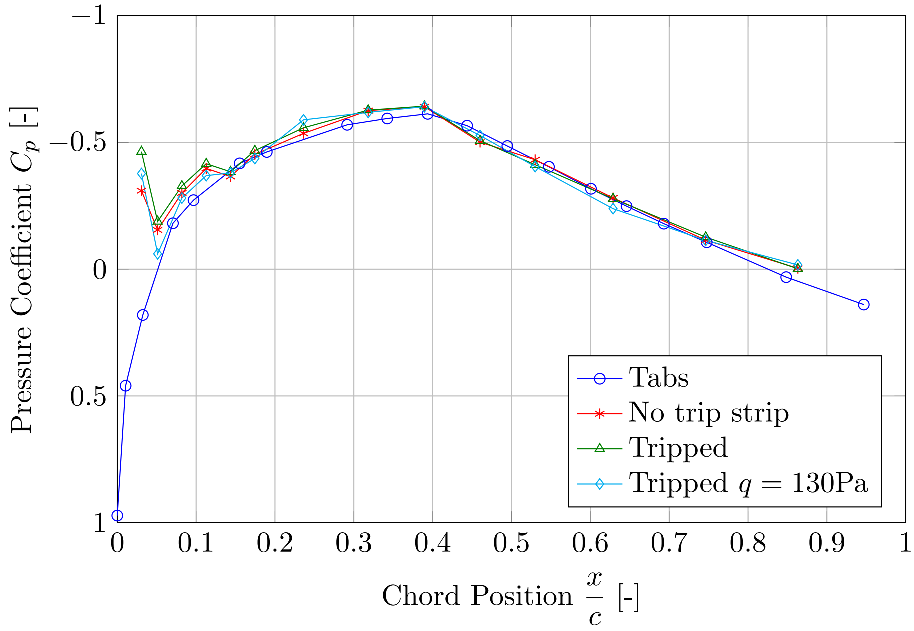

Figure 5.9: Comparison of pressure distribution measured with pressure tabs and straight MEMS pressure strip covered by cellophane, including trip strip of 0.40mm at 3-5% chord.

straight configuration was the better of the original setups. The results of the straight placement covered by cellophane is given in Figure 5.9.

The foil covered straight sensor gave the best comparison with the pressure tabs of all configurations tested. All three cases show agreement on the minimum C_p location at about 0.4 $^x/_c$, but are overpredicting it by 5%. A reason for the overprediction may be caused by the placement of the sensors on the wing surface. The sensors, tape and cellophane have a thickness of 1.27mm, which by placing on an 18% thick 250mm chord results in an increase of 0.5% in the thickness to chord ratio. An indication of the thickness increase on the airfoil is given in Figure 5.10. The modified airfoil shape was created using CAD software by placing a 1.27mm thickness increase at each sensor location. At the leading and trailing edge the lines were smoothly blended onto the original airfoil shape.

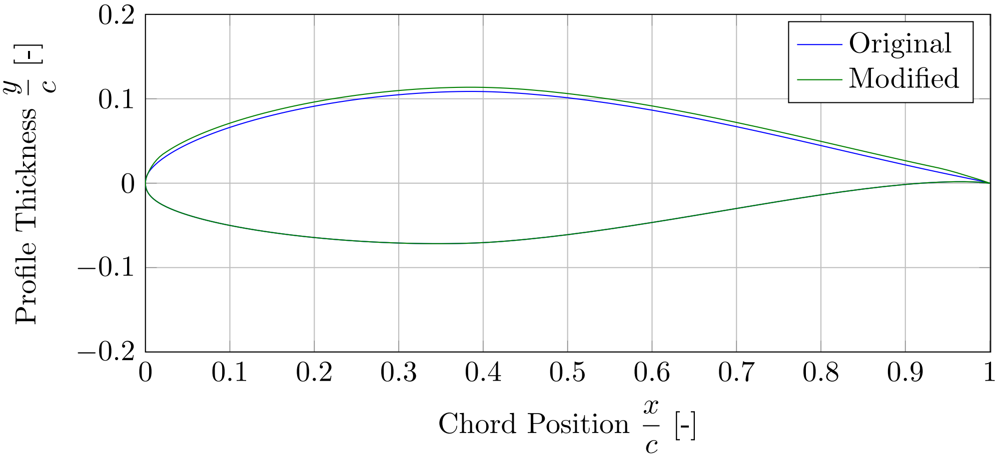

Figure 5.10: The NACA-64418 compared to the modified profile created by the addition of the pressure strip.

Although the computation of the two-dimensional lift curve is not possible because the pressure on the lower surface was not measured and the angle of attack is unknown, some indication of the thickness effect on pressure distribution can be seen when a two-dimensional analysis is performed on the original and modified airfoils.

Table 5.1: Xfoil settings for 2D analysis of both the NACA-64418 and the modified airfoil

Angle of attack [deg]	-5.0, -4.9, ..., 5.0
Mach number	0
Reynolds number	$0.5 \cdot 10^6$
Forced transition [x/c]	0.03
Panels upper/lower surfaces	103

The results of the pressure distributions for the upper surface of the NACA-64418 and the modified airfoil for an angle of attack of zero degrees is given in Figure 5.11.

The results in Figure 5.11 show a difference between the two pressure coefficients over the entire chord, with the modified thicker profile having a lower value. At the minimum pressure coefficient location $^x/_c = 0.4$ of the NACA-64418 the difference between the two airfoils is about 2%. The difference between the pressure distributions of the two airfoils are plotted for a range of angle of attacks in Figure 5.12.

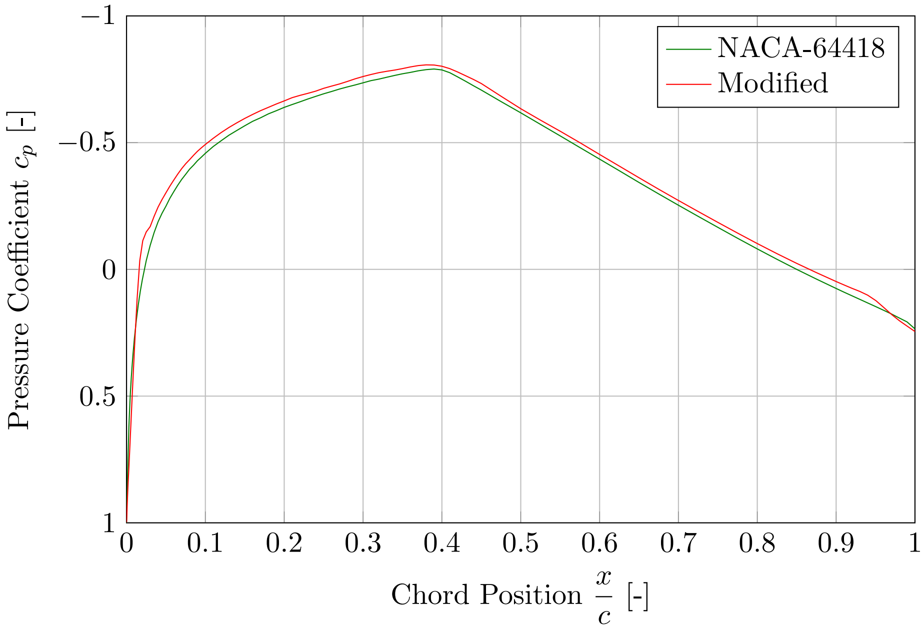

Figure 5.11: Upper surface pressure distribution for the NACA-64418 and the modified airfoil obtained from Xfoil.

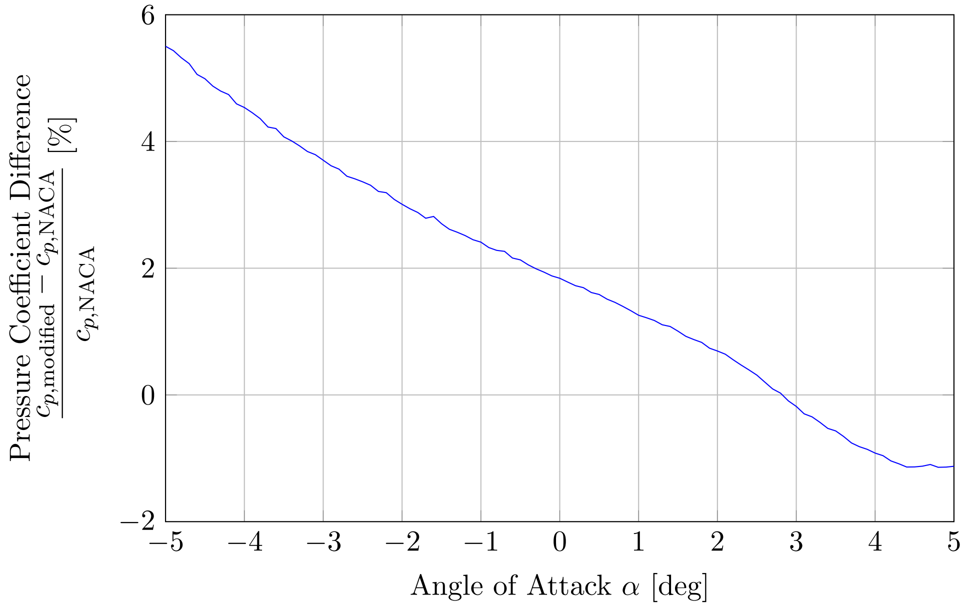

Figure 5.12: Pressure distribution difference at $\frac{x}{c} = 0.4$ *of the NACA-64418 and modified airfoils.*

Although not directly related to the actual pressure measurements it is clear from Figure 5.12 that there is an error introduced due to the thickness increase at all angles of attack with exception of approximately an angle of attack of 2.8 degrees where the error is zero. Such a thickness increase in percentage is much lower if the system is applied on, for example, the V3 kite for example. The V3 kite has a center chord of 2.60m and a maximum thickness to chord ratio of 9.5% this results in a thickness increase of 0.05%, a factor 10 smaller than the validation case.

There are additional discrepancies at the front and aft of the airfoil. A reason for these discrepancies is the flow transition from a laminar boundary layer to a turbulent boundary layer. The first sensor was placed exactly behind the trip strip, and from Figure 5.4 it is clear that disturbances occur due to the placement of the trip strip. But since the discrepancy is present even without the trip strip it is a pressure strip disturbance. Comparing the results of the final (Figure 5.9) and initial setup (Figure 5.6), the first pressure coefficient is approximately the same at about -0.5, this indicates that the first transition is still not smooth leading to faulty readings. In the case of the discrepancy at the aft of the wing section, this is similar to what has been observed by previous work[36]. It could be caused by the larger relative thickness increase locally compared to the airfoil thickness.

A closer look at the difference between the two measuring methods is given in Figure 5.13, where the pressure tabs data is linearly interpolated to obtain an estimate at the MEMS sensor locations. The dashed lines indicate the ±5% error which are considered acceptable in experiments.

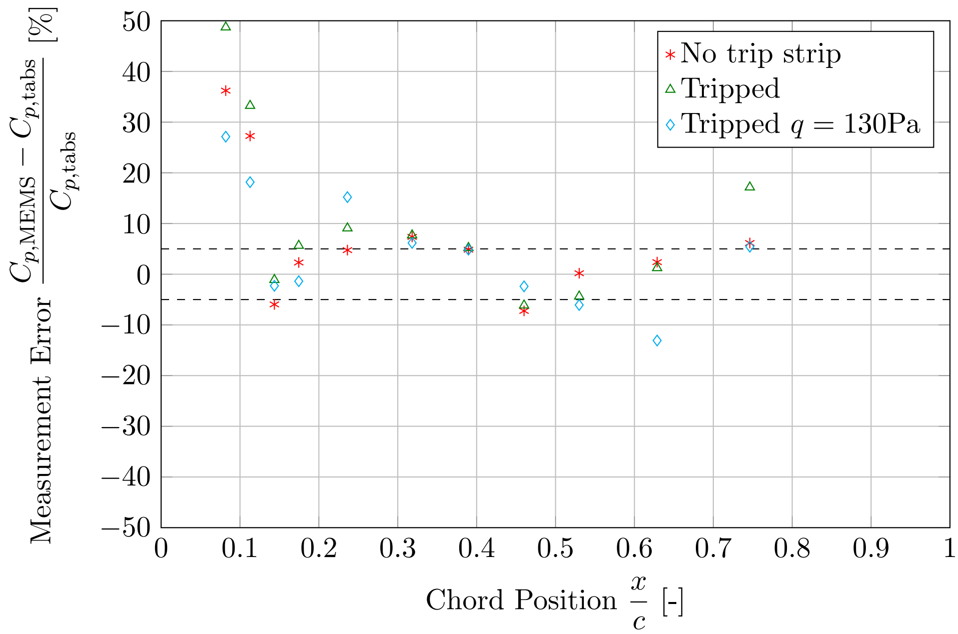

Figure 5.13: Measurement errors for the straight cellophane covered MEMS pressure sensors compared to the pressure tabs, including trip strip of 0.40mm at 3-5% chord.

What can be seen in the measurement errors first of all is that the first two and the last measurement points are outside the range of the graph, these errors are larger than 100%. The results are quite similar for the three cases, with positions having equal error. To determine in which configuration the measurements were the most accurate, the mean absolute error is compared for the three cases and is given in Table 5.2. Note that the first

Table 5.2: Mean absolute error for the straight placement of the cellophane covered MEMS pressure sensors, neglecting sensor 1,2 and 14, and including trip strip of 0.40mm at 3-5% chord..

	Mean absolute error [%]
No trip	9.52
Tripped	12.69
Tripped $q = 130$Pa	9.29

two and the last measurement points are omitted from these error calculations, although if included the ranking remained the same.

It was expected that the sensor error at lower velocities would have more impact on the results due to their measured value independency (see Section 3.3), this was not the case for the straight sensors with cellophane. One possible cause of this can be found in the degree of turbulence of the flow, as the sensors may cause vortices due to their protrusion into the flow field. Even though it is not a measure of the turbulence, the standard deviation of the data can give an indication whether there are pressure fluctuations present. Figure 5.14 gives the standard deviation for each individual sensor during the different testing configurations and for the ambient measurements.

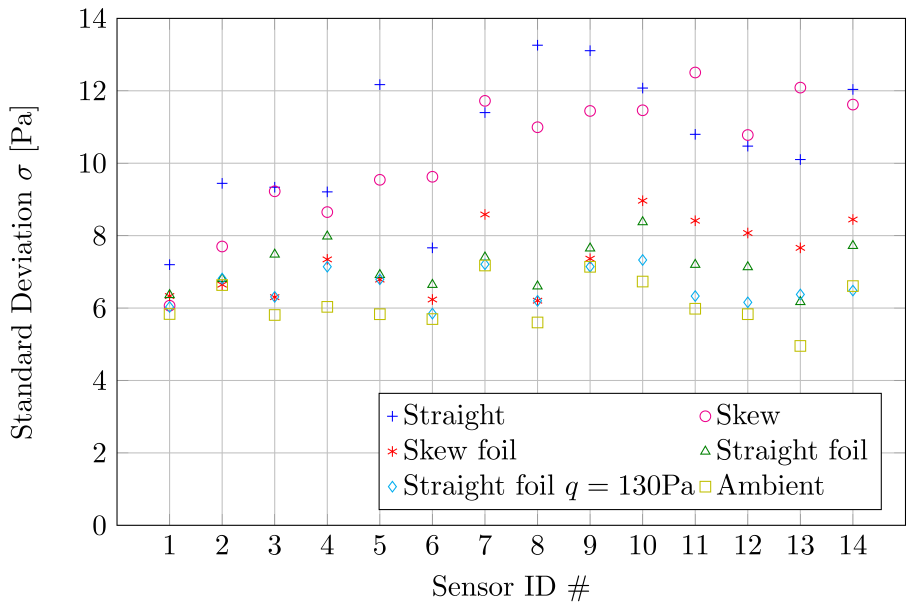

Figure 5.14: Standard deviation for the different sensors and setup configuration, foil indicates the presence of the cellophane cover.

By comparing the results for the straight foil at the different dynamic pressures, it is clear that the lower dynamic pressure results in a lower standard deviation, which would mean a more stable measurement. This difference also highlights the fact that the cellophane, although helpful, does not completely eliminate the presence of sharp corners and edges which cause vortices. Additionally what can be seen from the difference in the standard deviation is that the first sensor has the lowest for all configurations, which is what is expected as there are no disturbances upstream of it. The straight and skewed sensors without cellophane have the highest standard deviations which could directly be related to the small vortices shed from the upstream sensors. The final value of interest is the ambient pressure measurement difference between the before and after wind tunnel operations, this could indicate whether there is hysteresis in the sensors. The difference in the ambient pressure measurements for the straight sensors with cellophane are given in Figure 5.15.

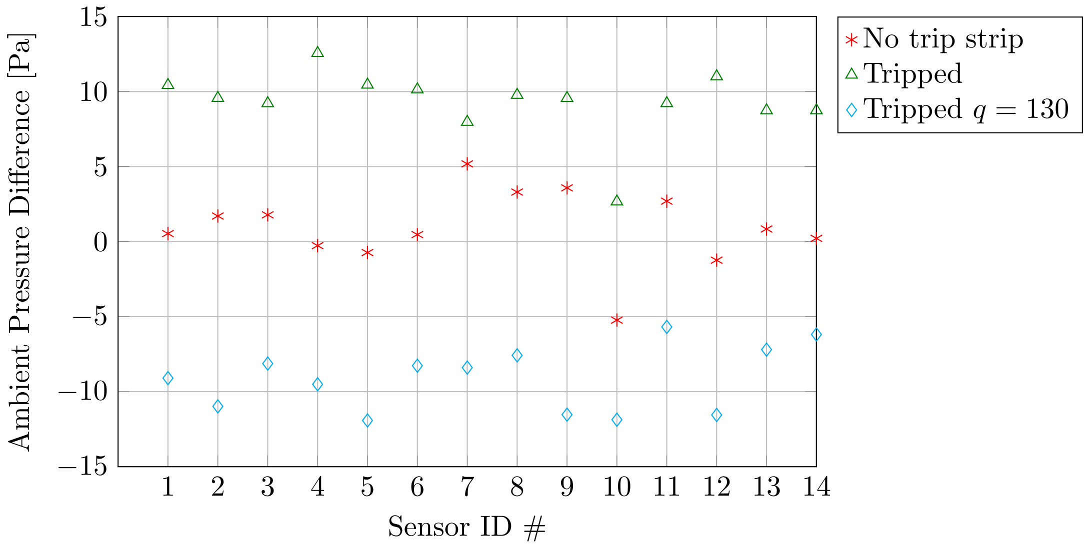

Figure 5.15: Difference between the static measurements before and after the wind tunnel was operated, taken for the same data set as Figure 5.9.

The sensors do not exhibit any hysteresis as for each of the runs the sensors show the same behavior with different average values. The difference of 10Pa can be directly attributed to ambient pressure fluctuations during the wind tunnel operations. Also the difference within the same run does not show differences larger than 10Pa which is smaller the accuracy indicated by the manufacturer of ±20Pa (see Table 3.1).

Chapter 6

Conclusions and Recommendations

Up to now, the pneumatic system developed by CSEM was the only suitable off-the-shelf system available for in-flight pressure measurements on flexible structures such as kites. However, pneumatically based systems requiring large tubing suffer from acoustic lag, and the stiffness required from the tubes to prevent kinks from occurring affect the flexibility of the kite. Therefore, the choice was made to develop a system based on MEMS (Micro-Electro-Mechanical Systems) sensors.

Of the different MEMS sensors considered, the LPS25H by STMicroelectronics was chosen. The validation of the prototype LPS25H sensors showed that their accuracy is in accordance with the specifications of the manufacturer. The sensors were integrated onto a flexible PCB (Printed Circuit Board), resulting in a strip which is easy to place onto the kite's surface, while maintaining maximum flexibility such that the dynamics of the canopy are not affected. The maximum data rate achieved for a strip with sixteen sensors and an internal averaging sample of 128 is 39Hz, while an individual sensor can be queried at 88Hz for the same sample number.

The validation of the performance of the pressure strip on an NACA-64418 wing section in direct comparison with pressure tabs performed in an open-jet low speed wind tunnel showed that the direct placement of the strip on the wing overestimated the pressure coefficient. This is the result of disturbances induced in the flow by the upstream sensors and the abrupt height change at the position of the sensors. Smoothing the area between the sensors by the placement of cellophane improved the performance of the system. The MEMS pressure strip covered by cellophane predicted the minimum C_p to within 5% of the pressure tabs, and the center section of the airfoil (from 15% up to 65% of the chord) to within $\pm 5\%$. There are still some discrepancies between the two measurement systems near the leading and trailing edge of the wing section, which can be attributed to the larger relative thickness of the sensors compared to the airfoil thickness at these locations. These however could be solved by making smoother pressure sensor strips by other means than the cellophane cover used here. Because the cellophane was stretched over the sensors there was still some sag between the sensors, therefore not creating a completely smooth surface. The circuit board could for example be filled up with a flexible polymer or silicone to the height of a sensor, resulting in a single thickness unit.

The implementation of the MEMS pressure strip onto the KitePower demonstrator kite requires a pitot-static tube to collect the reference pressures. On the designed pitot-static unit three types of systematic errors were identified:

1. Tip proximity to static ports causes lower static pressures.
2. The inclusion of the badminton shuttle increases the static pressure upstream.
3. The working principle of the selected differential pressure sensors allows a small amount of throughflow , resulting in lower measured dynamic pressures.

All the errors have been summarized in a single calibration curve, which can to correct the in-flight measured values.

In the end the MEMS pressure strip provides a lightweight solution for in-situ, in-flight pressure distribution measurements system for flexible lifting surfaces. The application of this system could give kite designers better insight into their designs and might increase the possibilities for improvements, which will contribute to the success of future kite power systems.

Recommendations

The are still some aspects of the pressure measuring strip that should be studied, such as:

- Quantify the effect of the increased profile thickness caused by the placement of the MEMS sensor strip.
- Investigate a better data/communication structure for the sensors to achieve higher data rates.
- Produce a better integrated smooth surface as replacement of the cellophane.

Recommendations with regard to the pitot-static tube system are:

- Integration of the pitot-static tube system into the same unit as the pressure measuring strip will allow easy deployability, without requiring the presence of the KCU (Kite Control Unit).
- Find or build an improved pitot-static tube with reduced tip proximity errors.
- Replace the differential pressure sensor with a sensor that does not allow throughflow, so that no additional errors are introduced.
- Determine the proper dimension of the badminton shuttle, to ensure proper alignment with the incoming flow throughout the entire kite flight envelope.

References

[1] Ockels, W. J., "Laddermill, a Novel Concept to Exploit the Energy in the Airspace," *Aircraft Design*, Vol. 4, No. 2-3, 2001, pp. 81–97.

[2] Van der Vlugt, R., Peschel, J., and Schmehl, R., "Design and Experimental Characterization of a Pumping Kite Power System," *Airborne Wind Energy*, edited by U. Ahrens, M. Diehl, and R. Schmehl, Green Energy and Technology, Springer Berlin Heidelberg, 2013, pp. 403–425.

[3] Loyd, M. L., "Crosswind Kite Power," *Journal of Energy*, Vol. 4, No. 3, 1980, pp. 106–111.

[4] Noom, M. N., *Theoretical Analysis of Mechanical Power Generation by Pumping Cycle Kite Power Systems*, Master's thesis, Delft University of Technology, 2013.

[5] Dictionary, O. E., *Oxford English Dictionary Online*, Oxford University Press, Oxford, UK `http://www.oed.com`, 2014, Retrieved January 20$^{\text{th}}$ 2014.

[6] Gunston, B., *The Cambridge Aerospace Dictionary (2nd Edition)*, Cambridge University Press, 2011.

[7] Breukels, J., *An Engineering Methodology for Kite Design*, Ph.D. thesis, Delft University of Technology, 2010.

[8] Hart, C., *Kites: An Historical Survey*, Paul P Appel, 1984.

[9] Fadul, J. A., *Kites in History, in Teaching and in Therapy*, Lulu Press, 2009.

[10] Schmehl, R., "Kite Power and Propulsion (AE4T40)," Lecture slides University of Technology Delft, 2011.

[11] Air, S. N. and Museum, S., "The Wright Broters, The Invention of the Aerial Age, Inventing a Flying Machine," Retrieved from `http://airandspace.si.edu/exhibitions/wright-brothers/online/fly/1899/kite.cfm`, December 10$^{\text{th}}$2013.

[12] "About Peter Powell Kites," Retrieved from http://www.peterpowellkites.co.uk/about/, January 30th2014.

[13] "Flexifoil Live to Fly," Retreived from http://www.flexifoil.com/about, January 30th 2014.

[14] "Setting the Altitude Record Straight," *Drachen Foundation Journal*, Vol. 21, 2006, pp. 8.

[15] "The Kiteboarding history," Retrieved from http://http://www.inflatablekite.com/siteinf/gb/InfHistory.html, February 15th2013.

[16] Van der Vlugt, R., Personal comunication, December 2012, Team rider and test pilot for Airush, and kite researcher at University of Technology Delft.

[17] Anonymous, "Ocean Rodeo: 2013 Razor SLE C kite," Retrieved from http://oceanrodeo.com/kiting/razor#tprod_venturi, November 21st 2012.

[18] U.S. Fish & Wildlife Service, "Peregrine Falcon (Falco peregrinus)," May 2006.

[19] Van den Heuvel, J., *Kitesailing: Improving System Performance and Safety*, Master's thesis, Delft University of Technology, 2010.

[20] Anonymous, "Ozone Seagull," Retreived from http://www.extremekites.com.au/forums/download/file.php?id=640&mode=view, April 20th 2014.

[21] Anonymous, "Naish Bolt," Retreived from http://www.briskites.com.au/images/products/large_628_11NaishBolt2.jpg, April 20th 2014.

[22] Anonymous, "Peregrine Falcon Diving," Retrieved from http://madyaba.com/peregrine-falcon-diving, May 26th2014.

[23] Anonymous, "Naish Helix," Retreived from http://www.bigwinds.com/images/products/naish/09/09-na-helix-s.jpg, April 20th 2014.

[24] Anonymous, "Seasmik," Retreived from http://i60.servimg.com/u/f60/14/00/70/66/0037w11.jpg, April 20th 2014.

[25] La Rocca, G., *Knowledge Based Engineering Techniques to Support Aircraft Design and Optimization*, Ph.D. thesis, Delft University of Technology, 2011.

[26] Pettersson, K. and Rizzi, A., "Aerodynamic scaling to free flight conditions: Past and present," *Progress in Aerospace Sciences*, Vol. 44, No. 4, 2008, pp. 295 – 313.

[27] De Wachter, A., *Deformation and Aerodynamic Performance of a Ram-Air Wing*, Master's thesis, Delft University of Technology, 2008.

[28] Van der Vlugt, R., *Aero- and Hydrodynamic Performance Analysis of a Speed Kiteboarder*, Master's thesis, Delft University of Technology, 2009.

[29] Ruppert, M. B., *Development and Validation of a Real Time Pumping Kite Model*, Master's thesis, Delft University of Technology, 2012.

[30] Costa, D., *Experimental Investigation of Aerodynamic and Structural Properties of a Kite*, Master's thesis, ETH Zurich, 2011.

[31] Maughmer, M., "A Comparison of the Aerodynamic Characteristics of Eight Sailwing Airfoil Sections," *NASA/SSA Science and Technology of Low-Speed and Motorless Flight*, No. 2085 in NASA CP, March 1979, pp. 155–176.

[32] Den Boer, R., "Numerical and Experimental Investigation of the Aerodynamics of Double Membrane Sailwing Airfoil Sections," Report LR 345, Delft University of Technology, February 1982.

[33] Marchaj, C. A., *Sail Performance*, Adlard Coles Nautical, 1996.

[34] Viola, I. M. and Flay, R. G., "Sail Pressures From Full-scale, Wind-tunnel and Numerical Investigations," *Ocean Engineering*, Vol. 38, No. 16, 2011, pp. 1733 – 1743.

[35] Rhode, R., "The Pressure Distribution over the Wings and Tail Surfaces of a Pw-9 Pursuit Airplane in Flight," Technical Report 364, NACA, 1931.

[36] Rivers, N. A., van Dam, C. P., Brown, P. W., and Rivers, R. A., "Flight Investigation of the Effects of Pressure-Belt Tubing Size on Measured Pressure Distributions," Technical Memorandum 209857, NASA, 2001.

[37] Burch, T., Schmid, N., Bitterli, S., Kathriner, S., Fengels, D., Sollberger, P., and Kressebuch, L., "A Customizable Pressure Strip for Rapid and in-situ Aerodynamics Testing," Scientific and Technical Report p. 72, CSEM, Neuchâtel, Switzerland, 2012.

[38] Holland, M., Eccles, L., and Paradis, L., "A Pressure Belt System for an Airborne Pressure Surveye," *Sensors for Industry, 2001. Proceedings of the First ISA/IEEE Conference*, IEEE, 2001, pp. 156 –161.

[39] Golfarelli, A., Zagnoni, M., Proli, P., Callegari, S., Talamelli, A., Sangiorgi, E., and Tartagni, M., "Acquisition System for Pressure Sensor Network," *Sensors IEEE*, Vol. 2, 2004, pp. 579–582, cited By (since 1996) 6.

[40] Egami, Y., Klein, C., Henne, U., Groot, K., Meyer, J., Krckeberg, C.-P., and Boden, F., "In-Flight Application of Pressure Sensitive Paint," *Advanced In-Flight Measurement Techniques*, edited by F. Boden, N. Lawson, H. W. Jentink, and J. Kompenhans, Research Topics in Aerospace, Springer Berlin Heidelberg, 2013, pp. 237–267.

[41] Liu, T., *Pressure- and Temperature-Sensitive Paints*, John Wiley & Sons, Ltd, 2010.

[42] Whitmore, S. and Leondes, C., "Compensating for Pneumatic Distortion in Pressure Sensing Devices," *Aerospace Sciences Meetings*, American Institute of Aeronautics and Astronautics, January 1990.

[43] Whitmore, S. A., "Formulation of a General Technique for Predicting Pneumatic Attenuation Errors in Airborne Pressure Sensing Devices," Technical Memorandum 100430, NASA, 1988.

[44] Yoshida, A., Tamura, Y., and Kurita, T., "Effects of Bends in a Tubing System for Pressure Measurement," *Journal of Wind Engineering and Industrial Aerodynamics*, Vol. 89, No. 1415, 2001, pp. 1701 – 1716, Bluff Body Aerodynamics and Applications.

[45] Anderson, J. D., *Fundamentals of Aerodynamics*, McGraw-Hill International Editions, 4th ed., 2005.

[46] Aerodynamics Research Group, "M-tunnel," Retrieved from `http://www.lr.tudelft.nl/en/organisation/departments/aerodynamics-wind-energy-flight-performance-and-propulsion/wind-tunnel-laboratories/low-speed-tunnels/m-tunnel/`, on March 13th 2014.

[47] Mensor, *Mensor Digital Pressure Gauge Series 2100 Operation Manual*, 2005.

[48] Mensor, *Operating Instructions Digital Pressure Gauge DPG 2400 Series*, July 2013.

[49] Van der Vlugt, R., Schmehl, R., and Noom, M. N., "Quasi-Steady Model of a Pumping Kite Power System," submitted to Renewable Energy.

[50] Sensirion, *SDP1000 / SDP2000 Low Range Differential Pressure Sensor for Air and Non-Aggressive Gases*, v5 ed., February 2013, retrived from `http://www.sensirion.com/fileadmin/user_upload/customers/sensirion/Dokumente/DiffPressure/Sensirion_Differential_Pressure_SDP1000_SDP2000_Datasheet_V5.pdf`.

[51] Berzal Mejías, A., *Wind Sensor Implementation Design*, Master's thesis, Delft University of Technology, 2011.

[52] Barlow, J. B., Rae, W. H., and Pope, A., *Low-speed Wind Tunnel Testing*, Wiley New York, 1999.

[53] Koninklijk Nederlands Meteorologisch Instituut, "Daggegevens van het weer in Nederland," Online, `www.knmi.nl/kd/daggegevens/index.cgi`.

Appendix A

LPS25H Data Sheet

These pages have been extracted from the data sheet of the LPS25H. The data sheet is available online at `http://www.st.com/web/catalog/sense_power/FM89/SC1316/PF255230`. Last retrieved March 2014.

LPS25H

MEMS pressure sensor: 260-1260 hPa absolute digital output barometer

Datasheet - production data

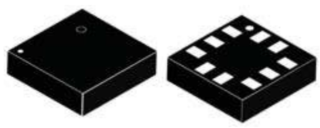

HCLGA-10L
(2.5 x 2.5 x 1.0 mm)

Features

- 260 to 1260 hPa absolute pressure range
- High-resolution mode: 1 Pa RMS
- Low power consumption:
  - Low resolution mode: 4 µA
  - High resolution mode: 25 µA
- High overpressure capability: 20x full scale
- Embedded temperature compensation
- Embedded 24-bit ADC
- Selectable ODR from 1 Hz to 25 Hz
- SPI and I²C interfaces
- Embedded FIFO
- Supply voltage: 1.7 to 3.6 V
- High shock survivability: 10,000 *g*
- Small and thin package
- ECOPACK® lead-free compliant

Applications

- Altimeter and barometer for portable devices
- GPS applications
- Weather Station Equipment
- Sport Watches

Description

The LPS25H is an ultra compact absolute piezoresistive pressure sensor. It includes a monolithic sensing element and an IC interface able to take the information from the sensing element and to provide a digital signal to the external world.

The sensing element consists of a suspended membrane realized inside a single mono-silicon substrate. It is capable to detect the absolute pressure and is manufactured with a dedicated process developed by ST.

The membrane is very small compared to the traditionally built silicon micromachined membranes. Membrane breakage is prevented by an intrinsic mechanical stopper.

The IC interface is manufactured using a standard CMOS process that allows a high level of integration to design a dedicated circuit which is trimmed to better match the sensing element characteristics.

The LPS25H is available in a cavity holed LGA package (HCLGA). It is guaranteed to operate over a temperature range extending from -30 °C to +105 °C. The package is holed to allow external pressure to reach the sensing element.

Table 1. Device summary

Order codes	Temperature range [°C]	Package	Packing
LPS25HTR	-30 to +105	HCLGA-10L	Tape and reel
LPS25H		HCLGA-10L	Tray

2 Mechanical and electrical specifications

2.1 Mechanical characteristics

V_{DD} = 2.5 V, T = 25 °C, unless otherwise noted.

Table 3. Mechanical characteristics

Symbol	Parameter	Test condition	Min.	Typ.[1]	Max.	Unit
Top	Operating temperature range		-30		105	°C
Tfull	Full accuracy temperature range		0		80	°C
Pop	Operating pressure range		260		1260	hPa
Pbits	Pressure output data			24		bits
Psens	Pressure sensitivity			4096		LSB/ hPa
Paccrel	Relative accuracy over pressure[2]	P = 800 to 1100 hPa T = 25°C		± 0.1		hPa
PaccT	Absolute accuracy pressure over temperature[3]	P = 260 to 1260 hPa T = 20 ~ +60 °C		± 0.2		hPa
		P = 260 to 1260 hPa T = 0 ~ +80 °C		± 1		
Pnoise	Pressure noise[4]	without embedded filtering		0.03		hPa RMS
		with embedded filtering		0.01		
Tbits	Temperature output data			16		bits
Tsens	Temperature sensitivity			480		LSB/°C
Tacc	Absolute accuracy temperature	T= 0 ~ +65 °C		± 2		°C

1. Typical specifications are not guaranteed.
2. Characterization data. Parameter not tested at final test
3. Embedded quadratic compensation.
4. Pressure noise RMS evalueted in a controlled environment,based on the average standard deviation of 32 measurements at highest ODR.

2.2 Electrical characteristics

VDD = 2.5 V, T = 25 °C, unless otherwise noted.

Table 4. Electrical characteristics

Symbol	Parameter	Test condition	Min.	Typ.(1)	Max.	Unit
VDD	Supply voltage		1.7		3.6	V
VDD_IO	IO supply voltage		1.7		3.6	V
Idd	Supply current @ ODR 1 Hz, highest resolution			25		µA
IddPdn	Supply current in power-down mode T = 25 °C			0.5		µA

1. Typical specifications are not guaranteed.

Appendix B

Electrical Components

This appendix contains the schematic drawings of the different electrical components that were required for the proper functioning of the designed system, including the actual MEMS sensor strip diagram.

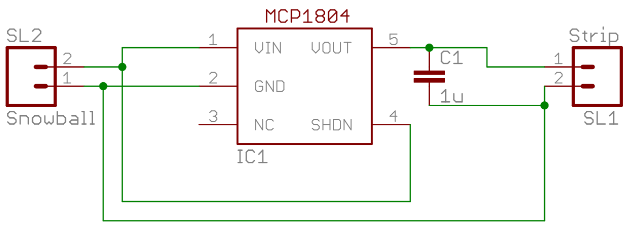

Figure B.1: schematic circuit drawing of voltage regulator used at Snowball supply voltage.

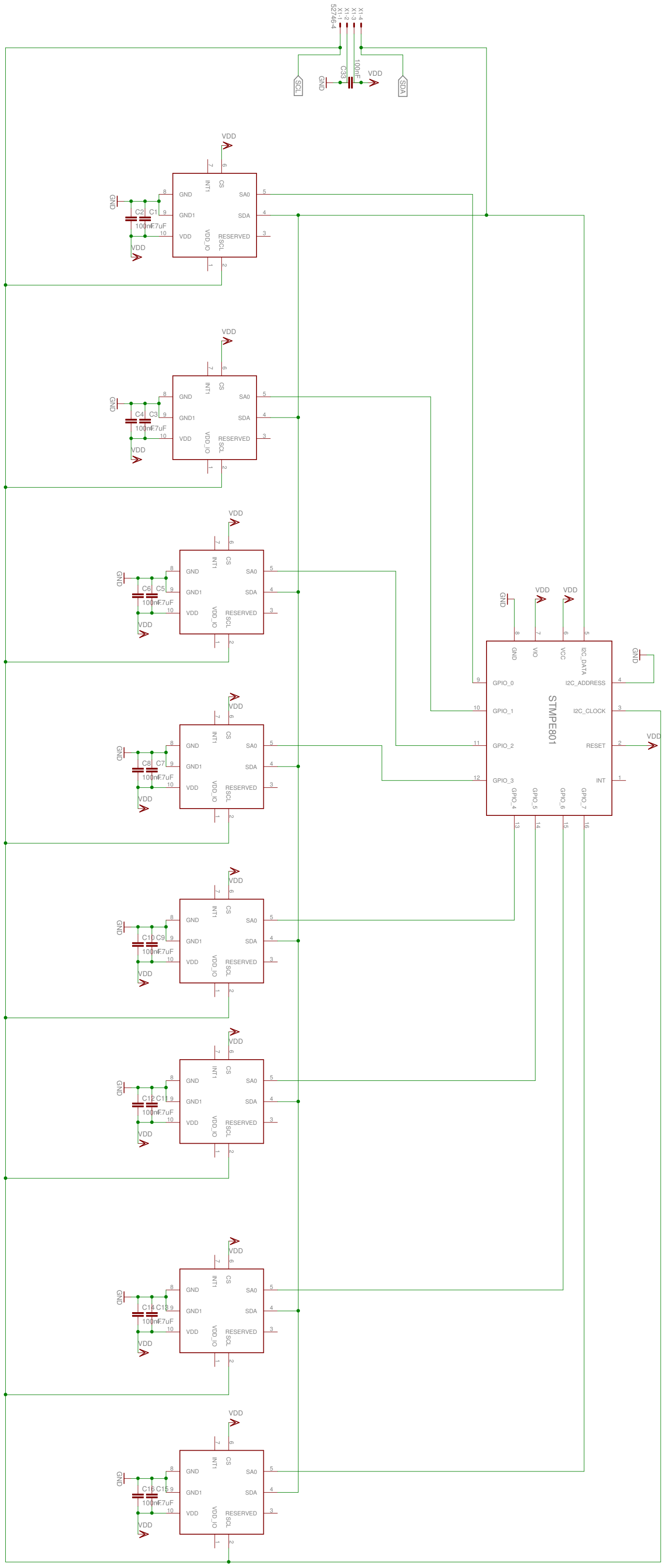

Figure B.2: One half of schematic circuit drawing of sensor array setup.

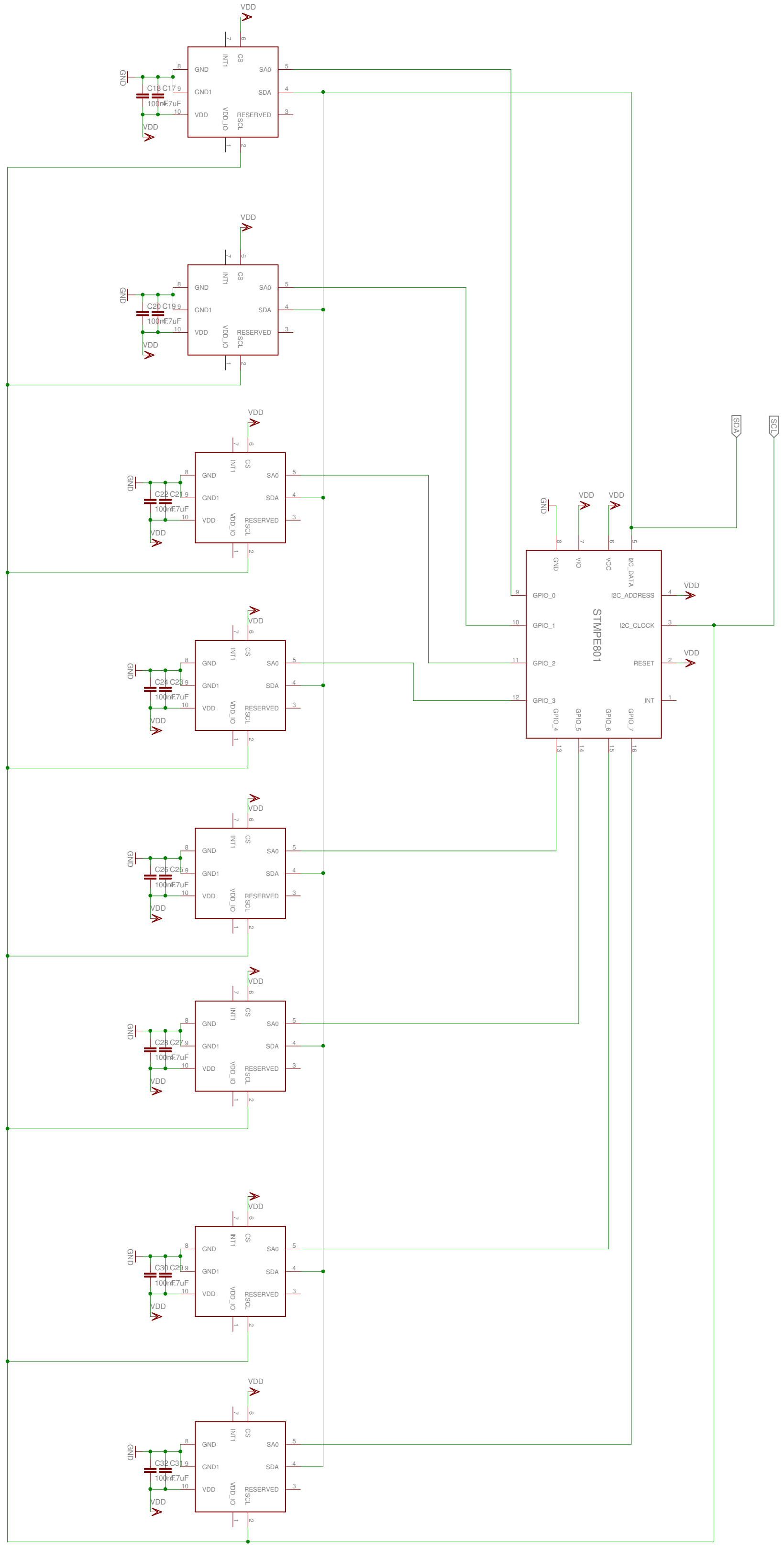

Figure B.3: Other half of schematic circuit drawing of sensor array setup.

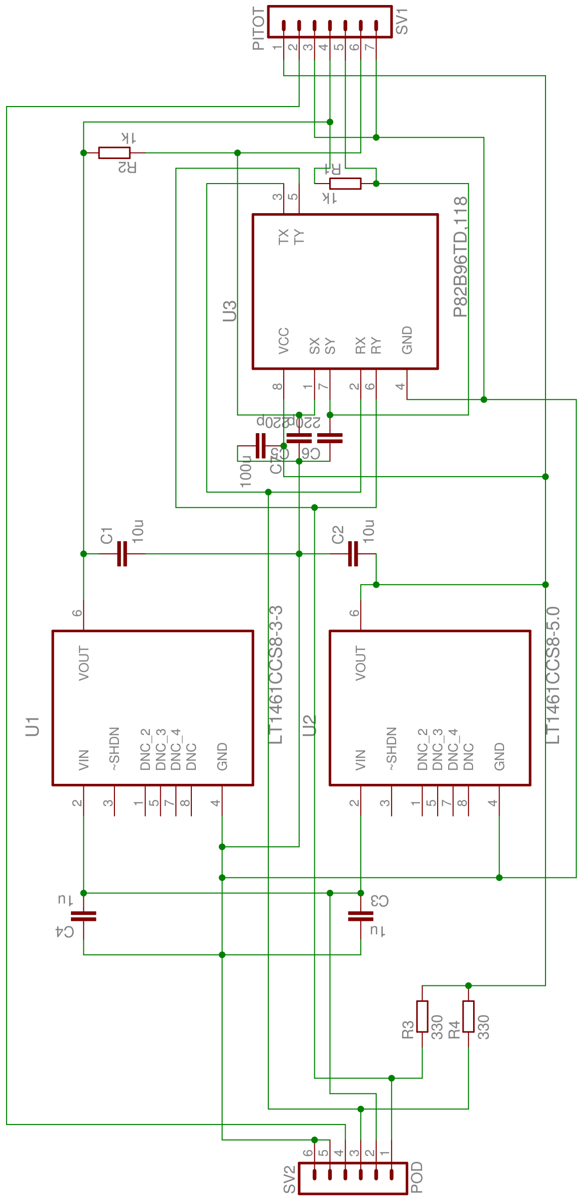

Figure B.4: Schematic circuit drawing of pitot connection near sensors.

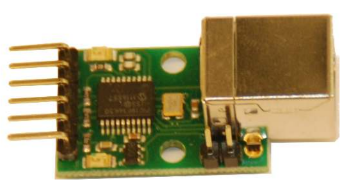

Figure B.5: USB-ISS adapter by robot-electronics used to give KCU I^2C capabilities.

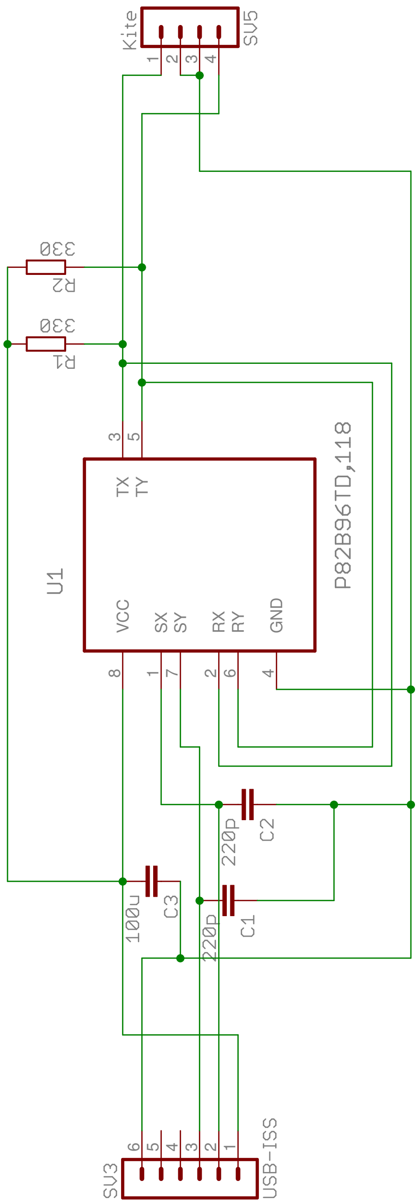

Figure B.6: Schematic drawing of the buffer chip connected to the USB-ISS module in the KCU.

Appendix C

Kite for CFD in Rhino

As an addition to this thesis a method was developed to create model of the kite designs. These can then be used in a wide range of computational models to perform CFD analysis.

C.1 Kite Model to GID Mesher

The original kite designs are made using Surfplan™. Due to the nature of the kite the single canopy needs to be converted into a "double" skin. This because the current FSI model being developed within the KitePower group requires a volume as input. The kite designs are exported from Surfplan™as **.dxf*, which can be imported into Rhinoceros® for geometric modifications.

The main differences between the modified and original kite designs besides the creation of the double skin are the removal of the struts including the tips, and the canopy is blended with the leading to create a smooth profile. Figure C.1 shows the original airfoil in blue which is generated by intersecting the kite with a cutting plane perpendicular to the leading edge at a leading edge segmentation. By offsetting the canopy 2mm in-ward the lower canopy surface is created. A smooth polyline is used to create the final airfoil shape indicated by the red line in Figure C.1. By performing this intersection and airfoil modification at each leading edge segmentation the different airfoils are defined. Figures C.2 to C.5 show the different views of the modified airfoils and the actual imported leading edge. Before the airfoils can be lofted they should be rebuild with equal number of control points in Rhinoceros® as this ensures a uniform loft by using the normal loft option in Rhinoceros®. The lofted kite can be seen in Figures C.6 to C.9 in red compared to the original Surfplan™kite. The complete loft is capped and exported as **.iges* file for further meshing in GID. Additionally the modified airfoils can be exported from rhino to panel method based computational models such as XFLR5 to create a kite planform together with the Surfplan™specifications of that kite.

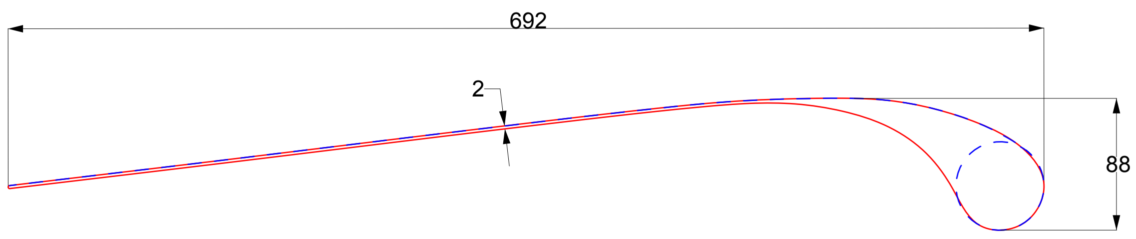

Figure C.1: Intersected airfoil in blue and modified airfoil in red (all dimensions in mm).

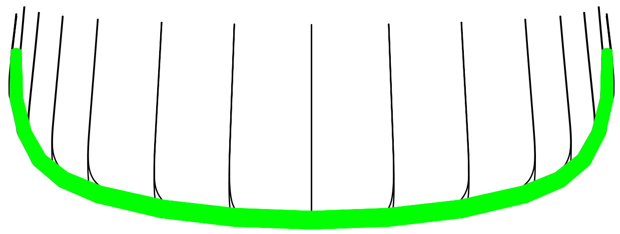

Figure C.2: Top view of the modified airfoils and the original leading edge.

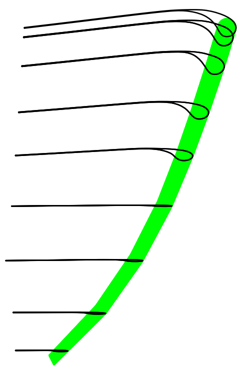

Figure C.3: Side view of the modified airfoils and the original leading edge.

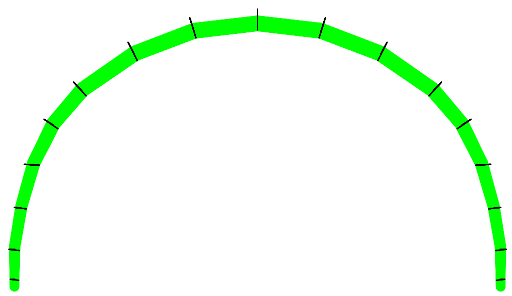

Figure C.4: Front view of the modified airfoils and the original leading edge.

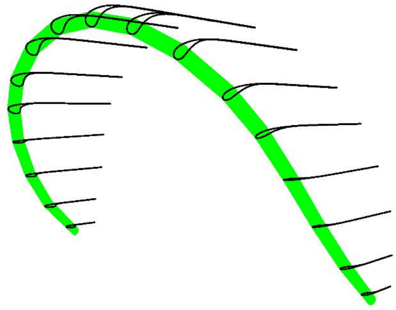

Figure C.5: Perspective view of the modified airfoils and the original leading edge.

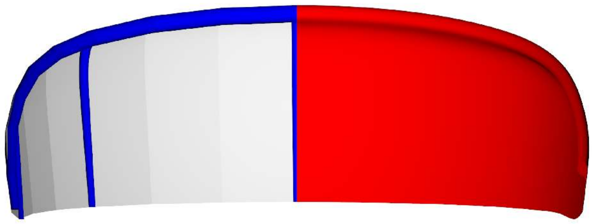

Figure C.6: Bottom view of the rendered "hybrid kite".

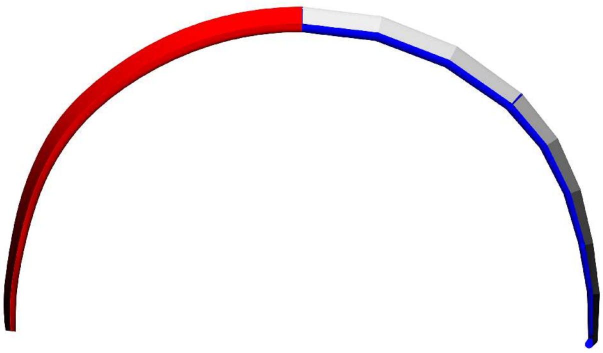

Figure C.7: Back view of the rendered "hybrid kite".

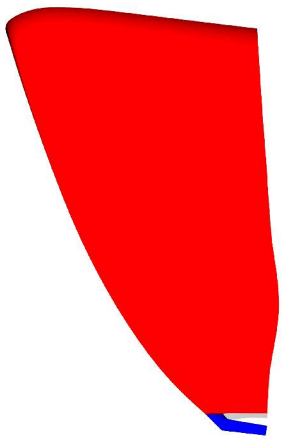

Figure C.8: Side view of the rendered "hybrid kite".

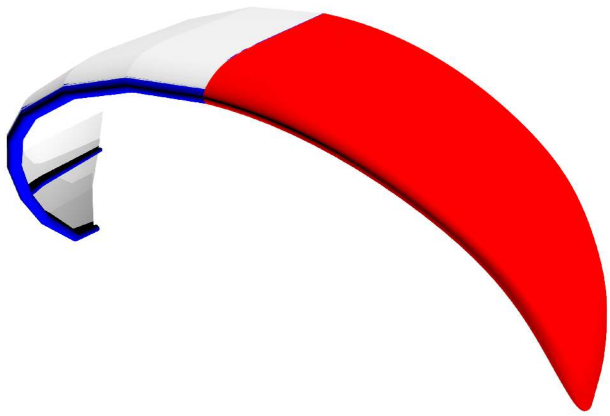

Figure C.9: Perspective view of the rendered "hybrid kite".